

ALMA INVESTIGATION OF VIBRATIONALLY EXCITED HCN/HCO⁺/HNC EMISSION LINES IN THE AGN-HOSTING ULTRALUMINOUS INFRARED GALAXY IRAS 20551–4250

MASATOSHI IMANISHI^{1,2}

Subaru Telescope, 650 North A'ohoku Place, Hilo, Hawaii, 96720, U.S.A.

KOUCIHIRO NAKANISHI²

National Astronomical Observatory of Japan, 2-21-1 Osawa, Mitaka, Tokyo 181-8588, Japan

AND

TAKUMA IZUMI

Institute of Astronomy, School of Science, The University of Tokyo, 2-21-1 Osawa, Mitaka, Tokyo 181-0015, Japan

Draft version November 15, 2021

ABSTRACT

We present the results of ALMA Cycle 2 observations of the ultraluminous infrared galaxy, IRAS 20551–4250, at HCN/HCO⁺/HNC J=3–2 lines at both vibrational-ground ($v=0$) and vibrationally excited ($v_2=1$) levels. This galaxy contains a luminous buried active galactic nucleus (AGN), in addition to starburst activity, and our ALMA Cycle 0 data revealed a tentatively detected vibrationally excited HCN $v_2=1$ f J=4–3 emission line. In our ALMA Cycle 2 data, the HCN/HCO⁺/HNC J=3–2 emission lines at $v=0$ are clearly detected. The HCN and HNC $v_2=1$ f J=3–2 emission lines are also detected, but the HCO⁺ $v_2=1$ f J=3–2 emission line is not. Given the high-energy level of $v_2=1$ and the resulting difficulty of collisional excitation, we compared these results with those of the calculation of infrared radiative pumping, using the available infrared 5–35 μ m spectrum. We found that all of the observational results were reproduced, if the HCN abundance was significantly higher than that of HCO⁺ and HNC. The flux ratio and excitation temperature between $v_2=1$ f and $v=0$, after correction for possible line opacity, suggests that infrared radiative pumping affects rotational (J-level) excitation at $v=0$ at least for HCN and HNC. The HCN-to-HCO⁺ $v=0$ flux ratio is higher than those of starburst-dominated regions, and will increase even more when the derived high HCN opacity is corrected. The enhanced HCN-to-HCO⁺ flux ratio in this AGN-hosting galaxy can be explained by the high HCN-to-HCO⁺ abundance ratio and sufficient HCN excitation at up to J=4, rather than the significantly higher efficiency of infrared radiative pumping for HCN than HCO⁺.

Subject headings: galaxies: active — galaxies: nuclei — quasars: general — galaxies: Seyfert — galaxies: starburst — submillimeter: galaxies

1. INTRODUCTION

The apparent ubiquity of supermassive blackholes (SMBHs) in the spheroidal components of present-day galaxies, and the correlation between the mass of SMBHs and spheroidal stellar components (Magorrian et al. 1998; Ferrarese & Merritt 2000; Gültekin et al. 2009; McConnell & Ma 2013) indicate that the active galactic nucleus (AGN; SMBH-driven activity) and the starburst (= active star-formation; plausibly the progenitors of spheroids) are physically connected and have co-evolved. Observational constraints on how and when SMBHs grow in mass, in relation to starbursts, is vital for fully understanding the galaxy formation process in the universe.

The widely accepted cold dark matter-based galaxy formation scenarios postulate that mergers of gas-rich galaxies with SMBHs at their centers are common throughout the history of the universe (Hopkins et al. 2008). Numerical simulations of such gas-rich galaxy mergers not only suggest that many stars form rapidly in

dust/gas-obscured regions, but also suggest that SMBHs have high mass accretion rates and become luminous AGNs, deeply buried in the nuclear dust/gas, making such gas-rich galaxy mergers luminous in the infrared (Hopkins et al. 2006). It is essential to evaluate the importance of *buried* AGNs in dust/gas-rich infrared luminous galaxy mergers, by separating them from the surrounding starbursts, if we are to observationally understand the physical processes that occur during this key epoch in the co-evolution of stars and SMBHs (Hopkins et al. 2005; Debuhr et al. 2011). However, unlike optically selected AGNs, where a central mass-accreting SMBH is surrounded by toroidally shaped dust/gas (the so-called dusty molecular torus) and the AGN's radiation can photo-ionize gas clouds along the torus axis above a torus scale height (Antonucci & Millar 1985), deeply buried AGNs are optically elusive and their detection requires observations at wavelengths of low dust extinction.

A buried AGN (mass accretion onto a SMBH) has two different properties from a starburst (nuclear fusion inside stars). First, the efficiency of the AGN's radiative energy generation (6–42% of $\dot{M}c^2$, where \dot{M} is the mass of the accreting material and c is the speed of light) (Bardeen 1970; Thorne 1974) is much higher than that of nuclear fusion inside stars ($\sim 0.7\%$ of $\dot{M}c^2$), so that an

Electronic address: masa.imanishi@nao.ac.jp

¹ National Astronomical Observatory of Japan, 2-21-1 Osawa, Mitaka, Tokyo 181-8588, Japan

² Department of Astronomical Science, The Graduate University for Advanced Studies (SOKENDAI), Mitaka, Tokyo 181-8588, Japan

AGN has very high surface brightness emission, and can heat a large amount of surrounding dust to high temperatures (several 100K), producing a strong mid-infrared 3–20 μm continuum emission. Second, the X-ray to UV luminosity ratio is much higher in an AGN than a starburst (Shang et al. 2011; Ranalli et al. 2003). These differences between an AGN and a starburst could create different effects/feedback to the surrounding material. If we discover AGN-sensitive (sub)millimeter molecular lines, we can disentangle the AGN from the starburst using the flux ratios of these lines, in a manner similar to the optical AGN-starburst spectroscopic classification method, based on the optical emission line flux ratios, which is extensively applied to less dusty galaxies (Veilleux & Osterbrock 1987; Kewley et al. 2001; Kauffmann et al. 2003). Once established, this (sub)millimeter molecular line energy diagnostic method will create a large potential to scrutinize deeply buried AGNs in dust/gas-rich galaxies out to the distant universe, because of (a) negligible dust extinction in the (sub)millimeter wavelength range, and (b) the availability of highly sensitive ALMA observing facility.

Based on pre-ALMA (sub)millimeter interferometric 1–5" resolution observations of the nuclear regions of nearby bright starburst and Seyfert galaxies (= modest luminosity AGNs), the enhanced emission of the dense gas tracer, HCN, at J=1–0 (rotational transition), relative to HCO^+ , has been found in AGNs and been proposed as a possible AGN indicator (Kohno 2005; Krips et al. 2008). This was mainly thanks to the spatially-resolved investigation of AGN-affected molecular gas, by reducing the contamination from spatially-extended star-formation-affected molecular gas emission in Seyfert host galaxies, because the contamination could hamper the detection of the signatures of AGN-affected molecular gas emission in large-aperture single-dish telescope observations (Gracia-Carpio et al. 2006; Baan et al. 2008; Snell et al. 2011; Costagliola et al. 2011). Subsequent interferometric observations have also confirmed enhanced HCN J=1–0 emission in the nuclei of dust/gas-rich merging luminous infrared galaxies (LIRGs; $L_{\text{IR}} > 10^{11} L_{\odot}$), which are diagnosed to be buried-AGN-important based on infrared spectroscopy, compared to starburst-dominated LIRGs (Imanishi et al. 2004, 2006; Imanishi & Nakanishi 2006; Imanishi et al. 2007a, 2009a). Based on recent single-dish telescope's observations, a similar trend of HCN J=1–0 flux excess, relative to HCO^+ J=1–0, has been confirmed for infrared-classified AGN-important LIRGs, compared to starburst-dominated LIRGs (Privon et al. 2015). ALMA Cycle 0–1 interferometric observations further support HCN emission enhancement, relative to HCO^+ , in the nuclei of AGN-important LIRGs, compared to starburst regions at J=4–3 (Imanishi & Nakanishi 2013a,b; Iono et al. 2013; Imanishi & Nakanishi 2014; Garcia-Burillo et al. 2014; Izumi et al. 2015). It has now become clear that luminous AGNs tend to show enhanced HCN emission. However, the physical interpretation of enhanced HCN emission in AGNs is still unclear. Although HCN abundance enhancement in an AGN is proposed in some chemical calculations, because of high dust temperature and/or X-ray irradiation (Meijerink & Spaans 2005; Lintott & Viti 2006; Harada et al. 2010), it is also calculated that the HCN-to- HCO^+ abundance ratio in molecular gas around an AGN can vary

dramatically, depending on assumed physical parameters (Meijerink & Spaans 2005; Harada et al. 2013). Additionally, even if HCN abundance is indeed enhanced in an AGN, the widely assumed collisional excitation alone seems not to be enough to reproduce the strong HCN rotational J-transition emission lines observed in some AGNs (Yamada et al. 2007).

An infrared radiative pumping mechanism has been proposed to be a plausible scenario for the enhancement of HCN rotational J-transition emission in AGNs (Aalto et al. 1995; Garcia-Burillo et al. 2006; Weiss et al. 2007). Specifically, HCN can be vibrationally excited to $v_2=1$ by absorbing infrared 14 μm photons (Townes & Schawlow 1975). Through the decay back to the vibrational-ground level ($v=0$), the HCN rotational J-transition flux at $v=0$ can be stronger than collisional excitation alone (Rangwala et al. 2011). Since an AGN can emit infrared 14 μm continuum emission much more strongly than a starburst, due to AGN-heated hot (several 100 K) dust, such an infrared radiative pumping mechanism for HCN should work more effectively in an AGN than in a starburst. In fact, the HCN $v_2=1-0$ *absorption* features were seen at infrared 14 μm in several obscured AGNs (Lahuis et al. 2007), and the vibrationally excited HCN $v_2=1, l=1f$ (hereafter $v_2=1f$) J=4–3 and/or J=3–2 *emission* lines in the (sub)millimeter wavelength have recently been detected in several AGN-hosting LIRGs (Sakamoto et al. 2010; Imanishi & Nakanishi 2013b; Aalto et al. 2015a,b; Costagliola et al. 2015), supporting the scenario that infrared radiative pumping actually works in some AGNs to vibrationally excite HCN and could contribute to an increase in HCN J-transition flux at $v=0$.

However, the other dense gas tracers, HCO^+ and HNC, also have absorption features at infrared $\sim 12 \mu\text{m}$ and $\sim 21.5 \mu\text{m}$, respectively (Davies et al. 1984; Kawaguchi et al. 1985; Burkholder et al. 1987), and could therefore be vibrationally excited to $v_2=1$ by infrared radiative pumping. If the infrared radiative pumping mechanism is responsible for the enhanced HCN J-transition emission at $v=0$ in AGNs, its efficiency must be particularly high for HCN only. A comparison of the strengths of the $v_2=1$ emission lines for HCN, HCO^+ , and HNC is the most straightforward way to test the scenario of whether infrared radiative pumping works most efficiently for HCN and selectively boosts HCN J-transition flux at $v=0$. No meaningful observational constraints are placed in external galaxies for the strengths of HCO^+ and HNC $v_2=1f$ J-transition lines, except for the report concerning the detection of HNC $v_2=1f$ J=3–2 emission line in the AGN-hosting LIRG, NGC 4418 (Costagliola et al. 2013).

We conducted ALMA Cycle 2 observations of the luminous infrared galaxy, IRAS 20551–4250 ($z=0.043$), to investigate the relative strength of vibrationally excited ($v_2=1$) HCN, HCO^+ , and HNC J-transition lines. IRAS 20551–4250 is categorized as an ultraluminous infrared galaxy (ULIRG) with infrared (8–1000 μm) luminosity $L_{\text{IR}} = 10^{12.0} L_{\odot}$, and has far-infrared (40–500 μm) luminosity $L_{\text{FIR}} = 10^{11.9} L_{\odot}$ (see Table 1 of Imanishi & Nakanishi 2013b). It consists of main single nucleus with the signature of a long merging tail in the southern direction (Duc et al. 1997; Rothberg & Joseph 2004). It is classified optically as a LINER/HII-region; namely, it has no obvious optical AGN (Seyfert) signature (Duc et al. 1997; Yuan et al. 2010). Based on

several energy diagnostic methods using infrared and X-ray spectroscopy, the signature of a luminous, energetically significant (20–60% of the bolometric luminosity) buried AGN was identified in IRAS 20551–4250, in addition to starburst activity (Franceschini et al. 2003; Risaliti et al. 2006; Sani et al. 2008; Nardini et al. 2008, 2009, 2010; Imanishi et al. 2010a, 2011; Veilleux et al. 2013). The vibrationally excited HCN $v_2=1f$ J=4–3 emission line was tentatively detected with our ALMA Cycle 0 data because of small molecular line widths, which enable us to clearly separate the HCN $v_2=1f$ J=4–3 emission line from the nearby, much brighter, HCO⁺ $v=0$ J=4–3 emission line (Imanishi & Nakanishi 2013b). Thus, IRAS 20551–4250 is a very good target for investigating the relative strength of vibrationally excited HCN/HCO⁺/HNC J-transition emission lines, and how the infrared radiative pumping mechanism affects the rotational excitation of HCN/HCO⁺/HNC at $v=0$.

In the present paper, we report the results of ALMA Cycle 2 observations of the AGN-hosting ULIRG, IRAS 20551–4250, at HCN, HCO⁺, and HNC lines at both the vibrational-ground ($v=0$) and vibrationally excited ($v_2=1$) levels. Throughout this paper, we adopt $H_0 = 71 \text{ km s}^{-1} \text{ Mpc}^{-1}$, $\Omega_M = 0.27$, and $\Omega_\Lambda = 0.73$ (Komatsu et al. 2009), in which case the luminosity distance is 188 Mpc and 1 arcsec corresponds to 0.84 kpc at the distance of IRAS 20551–4250. Molecular parameters are derived from the Cologne Database of Molecular Spectroscopy (CDMS) (Müller et al. 2005) via Splatalogue (<http://www.splatalogue.net>). For molecular transitions, where there is no indication of v (the vibrational-level), we mean $v=0$ (i.e., the vibrational-ground level). When we write HCN, HCO⁺, and HNC in this manuscript, we mean H¹²C¹⁴N, H¹²C¹⁶O⁺, and H¹⁴N¹²C, respectively.

2. OBSERVATIONS AND DATA ANALYSIS

Our ALMA Cycle 2 observations in band 6 (211–275 GHz) were undertaken within the program 2013.1.00033.S (PI = M. Imanishi). The details of our observations are given in Table 1. We adopted the widest 1.875 GHz band mode and 3840 total channel number for our observations. We requested $<0''.6$ spatial resolution in our proposal.

We employed three spectral windows in USB in band 6 to cover (a) HCN J=3–2 (rest-frame frequency is $\nu_{\text{rest}} = 265.89 \text{ GHz}$), (b) HCO⁺ J=3–2 ($\nu_{\text{rest}} = 267.56 \text{ GHz}$) and HCN $v_2=1f$ J=3–2 ($\nu_{\text{rest}} = 267.20 \text{ GHz}$), and (c) HCO⁺ $v_2=1f$ J=3–2 ($\nu_{\text{rest}} = 268.69 \text{ GHz}$) in each of the three spectral windows. HCN and HCO⁺ J=3–2 emission lines can therefore be obtained at both the vibrational-ground ($v=0$) and vibrationally excited ($v_2=1f$) levels concurrently.

We also conducted additional independent observations for HNC J=3–2 ($\nu_{\text{rest}} = 271.98 \text{ GHz}$) and HNC $v_2=1f$ J=3–2 ($\nu_{\text{rest}} = 273.87 \text{ GHz}$). We employed four spectral windows, of which two in USB were used to cover HNC J=3–2 and HNC $v_2=1f$ J=3–2 lines. The remaining two spectral windows in LSB were used to probe continuum emission and serendipitously detected emission lines.

We used CASA (Petty et al. 2012) for our data analysis. We first checked the visibility plots in calibrated data provided by the Joint ALMA Observatory and found that

the presence of HCN, HCO⁺, and HNC J=3–2 emission lines was clearly recognizable. Signatures of other weak emission lines were also seen in some spectral windows. We selected channels that were not clearly affected by detected emission line features, and estimated the continuum flux levels, by using data in (a) three spectral windows for HCN/HCO⁺ observations and (b) four spectral windows for HNC observations. After subtracting these estimated continuum levels, we performed the task “clean” for detected emission line data. We applied the “clean” procedure also for the continuum data. We employed 40 channel spectral binning ($\sim 20 \text{ km s}^{-1}$), and adopted a pixel scale of $0''.1 \text{ pixel}^{-1}$ in this clean procedure. The maximum recoverable scale in our data is $\sim 10''$. In ALMA Cycle 2, the absolute calibration uncertainty is estimated to be $<10\%$ in band 6, which will not significantly affect our main discussion.

3. RESULTS

From our observations, two continuum data were obtained. Figure 1 displays continuum-a (taken with the HCN and HCO⁺ J=3–2 observations) and continuum-b (taken with HNC J=3–2) maps. Table 2 presents the continuum emission properties. The achieved spatial resolution is $\sim 0''.5$ ($\sim 420 \text{ pc}$) (Table 2, column 5) and meets our request of $<0''.6$. Using the CASA task “imfit”, we estimate the deconvolved, intrinsic emission size to be $0''.28 \times 0''.23$ ($240 \text{ pc} \times 190 \text{ pc}$) for continuum-a and $0''.28 \times 0''.24$ ($240 \text{ pc} \times 205 \text{ pc}$) for continuum-b, with the uncertainties of $<20 \text{ pc}$, where the values along the major and minor axes are shown. Continuum emission is estimated to have a spatial extent with about half of the ALMA synthesized beam size. These independently taken continuum data show consistent results, in terms of peak position, peak flux, and morphology. To understand the physical origin of the detected continuum emission, we assume that half of the far-infrared (40–500 μm) luminosity of IRAS 20551–4250 comes from starburst activity, because (a) the AGN bolometric contribution in IRAS 20551–4250 is estimated to be 20–60% (Nardini et al. 2008, 2009, 2010; Veilleux et al. 2013) and (b) the bolometric luminosity of IRAS 20551–4250 is dominated by far-infrared (40–500 μm) emission ($L_{\text{FIR}} = 10^{11.9} L_\odot$) (§1). The contribution from thermal free-free emission in starburst HII-regions at $\sim 255 \text{ GHz}$ is estimated to be $\sim 1.6 \text{ mJy}$, using equation (1) of Nakanishi et al. (2005). This is a significant contribution to the observed continuum flux at $\sim 255 \text{ GHz}$ with 3.6–3.8 mJy. If the starburst contribution to the observed far-infrared luminosity is higher than 50%, the free-free emission flux at $\sim 255 \text{ GHz}$ will be even higher. Therefore, we infer that the detected continuum emission (~ 3.6 – 3.8 mJy) at $\sim 255 \text{ GHz}$ is a combination of thermal free-free emission from starburst HII-regions and dust emission heated by dust-obscured energy sources (AGN and/or starburst). Since the detected continuum emission is spatially compact with $<250 \text{ pc}$ (Fig. 1), the thermal free-free emission should be of nuclear starburst origin.

A full spectrum taken with our ALMA observations at the continuum peak position within the beam size is shown in Figure 2. In the spectrum taken with HCN/HCO⁺ J=3–2 lines, the HCN $v_2=1f$ J=3–2 emission line is visible, but the HCO⁺ $v_2=1f$ J=3–2 line is not (Fig. 2c). In the spectrum taken with the HNC J=3–

2 line, the HNC $v_2=1f$ J=3–2 emission line is detected (Fig. 2e). We also serendipitously detected several other emission lines. In the spectrum taken with HCN/HCO⁺ J=3–2 lines, an emission line is recognizable at the observed frequency $\nu_{\text{obs}} \sim 257.40$ GHz, or rest-frame frequency $\nu_{\text{rest}} \sim 268.47$ GHz. We ascribe this emission line to HOC⁺ J=3–2 ($v=0$) at $\nu_{\text{rest}} = 268.45$ GHz, which was strongly detected in the Galactic star-forming regions (Apponi et al. 1997, 1999; Savage & Ziurys 2004) and LIRGs (Aalto et al. 2015a,b).

In the spectrum taken with the HNC J=3–2 line, emission lines are identifiable at $\nu_{\text{obs}} \sim 245.75$ GHz, 247.60 GHz, 248.35 GHz, 261.65 GHz, and 262.15 GHz. The third and fourth lines at $\nu_{\text{obs}} \sim 248.35$ GHz and 261.65 GHz correspond to the rest-frame frequencies of $\nu_{\text{rest}} \sim 259.0$ GHz and 272.9 GHz, which we ascribe to H¹³CN J=3–2 ($\nu_{\text{rest}} \sim 259.01$ GHz) and HC₃N J=30–29 ($\nu_{\text{rest}} \sim 272.88$ GHz) (Costagliola & Aalto 2010; Costagliola et al. 2013), respectively. The first and second lines at $\nu_{\text{obs}} \sim 245.75$ GHz and 247.60 GHz correspond to $\nu_{\text{rest}} \sim 256.3$ GHz and 258.2 GHz, which we tentatively attribute to SO₂ 5(3,3)–5(2,4) ($\nu_{\text{rest}} \sim 256.25$ GHz) and SO 6(6)–5(5) ($\nu_{\text{rest}} \sim 258.26$ GHz), respectively, because these lines are the strongest in these frequency ranges in the Galactic star-forming region, Orion A (Blake et al. 1986; Greaves & White 1991). For the second line, HC¹⁵N J=3–2 emission line ($\nu_{\text{rest}} \sim 258.16$ GHz) might make some contribution. For the fifth line at $\nu_{\text{obs}} \sim 262.15$ GHz, or $\nu_{\text{rest}} \sim 273.4$ GHz, we tentatively assign it as CH₃CCH 16(2)–15(2) ($\nu_{\text{rest}} \sim 273.40$ GHz), based on the extra-galactic detection in the Splatalogue database (<http://www.splatalogue.net>).

We note that the rest-frequencies of $v_2=1e$ J=3–2 for HCN ($\nu_{\text{rest}} = 265.85$ GHz), HCO⁺ ($\nu_{\text{rest}} = 267.42$ GHz), and HNC ($\nu_{\text{rest}} = 271.92$ GHz) are so close to the $v=0$ J=3–2 line for each molecule that it is very difficult to separate the $v_2=1e$ J=3–2 lines from the much stronger $v=0$ J=3–2 emission lines. The fluxes of the $v_2=1e$ emission lines of HCN/HCO⁺/HNC will not be discussed in this paper.

We create integrated intensity (moment 0) maps of individual molecular lines by combining channels with clear signal signs. Figure 3 displays these maps. Table 3 summarizes their properties. The achieved spatial resolution is $\sim 0''.5$ (~ 420 pc) for all molecular emission lines (Table 3, column 6), and so our request of $< 0''.6$ is fulfilled. The molecular line peak positions agree with the continuum emission peak within 1 pixel ($0''.1$) in RA and DEC directions for all lines, suggesting that several serendipitously detected faint emission lines are real. The estimated deconvolved, intrinsic emission sizes for the brightest HCN, HCO⁺, and HNC $v=0$ J=3–2 lines, using the CASA task "imfit", are $0''.22 \times 0''.20$ ($185 \text{ pc} \times 170 \text{ pc}$), $0''.27 \times 0''.26$ ($225 \text{ pc} \times 220 \text{ pc}$), and $0''.21 \times 0''.17$ ($175 \text{ pc} \times 145 \text{ pc}$), with the uncertainties of < 15 pc, respectively. HCO⁺ $v=0$ J=3–2 emission may show slightly larger spatial extension than HCN $v=0$ J=3–2 and HNC $v=0$ J=3–2 emission.

Figure 4 shows spectra around individual molecular lines of our interest at the continuum peak position within the beam size. We fit detected molecular emission lines in the spectra with Gaussian profiles. Table 3 summarizes the fitting results. The flux estimates based on the Gaussian fits will be used in our discussion, except

for the non-detected HCO⁺ $v_2=1f$ J=3–2 emission line for which the upper limit in the integrated intensity (moment 0) map is adopted. The molecular line luminosities are summarized in Table 4.

Intensity-weighted mean velocity (moment 1) and intensity-weighted velocity dispersion (moment 2) maps for HCN, HCO⁺, and HNC J=3–2 ($v=0$) emission lines are shown in Figure 5. In all moment 1 maps, the north-eastern region is redshifted and the southwestern region is blueshifted, with respect to the nucleus, suggesting a rotating gas motion. A similar gas motion was seen in HCN and HCO⁺ J=4–3 ($v=0$) emission lines (Imanishi & Nakanishi 2013b), suggesting that the spatial origin of these detected molecular emission lines is similar. A similar rotational gas motion is seen also at CO J=1–0 emission (Ueda et al. 2014), although the detected CO J=1–0 emission is distributed in a wider area than HCN, HCO⁺, and HNC, due to its lower critical density and higher brightness.

4. DISCUSSION

4.1. Molecular line flux ratio

In Figure 6, the observed HCN-to-HCO⁺ J=3–2 and HCN-to-HNC J=3–2 flux ratios of IRAS 20551–4250 are added to the plot for J=4–3 (Imanishi & Nakanishi 2014). The AGN-hosting ULIRG, IRAS 20551–4250, shows similar HCN-to-HCO⁺ flux ratios both at J=4–3 and J=3–2, and the ratios are higher than starburst-dominated regions.

Both the HCN-to-HCO⁺ and HCN-to-HNC flux ratios can change, depending on (a) abundance ratio resulting from various chemical reactions, (b) excitation condition, and (c) flux attenuation by line opacity. The flux comparison between J=4–3 (Imanishi & Nakanishi 2013b) and J=3–2 (Table 5) for HCN, HCO⁺, and HNC shows that the ratios of J=4–3 to J=3–2 flux in [Jy km s^{-1}] are 1.6 ± 0.2 for HCN, 1.7 ± 0.2 for HCO⁺, and 1.8 ± 0.2 for HNC, where maximum $\sim 10\%$ absolute calibration uncertainty in individual ALMA observations is included. These ratios are comparable to the expected ratio for thermally excited optically thick gas ($= 16/9$), which suggests that the excitation temperatures of HCN, HCO⁺, and HNC for J=3–2 and J=4–3 are comparable to the kinetic temperature of molecular gas in the nuclear region of IRAS 20551–4250. In general, when molecular gas density and temperature are not sufficiently high, collisional excitation at high-J levels can become sub-thermal more quickly and deviate from thermal condition more strongly for a molecule with higher critical density than another molecule with lower critical density. While HCN and HNC have comparable critical densities at individual J-transitions, HCO⁺ has a slightly lower critical density than HCN and HNC by a factor of ~ 5 for the same J-transition (Meijerink et al. 2007; Greve et al. 2009). Thus, the HCN-to-HCO⁺ flux ratio can be smaller at higher J-transition (e.g. J=4–3) than at lower J-transition (e.g., J=3–2) in some galaxies. The observed similar HCN-to-HCO⁺ and HCN-to-HNC flux ratios between J=4–3 and J=3–2 suggest that the different excitation condition for different molecules (item (b) above) is not an important factor for the ratios at J=3–2 and J=4–3 in IRAS 20551–4250. However, in other galaxies, sub-thermal excitation conditions can occur, in which case the observed HCN-to-HCO⁺ flux ratio

at J=4–3 (and J=3–2) can be smaller than that at J=1–0. This may be partly responsible for the small observed HCN-to-HCO⁺ J=4–3 flux ratios in starburst-dominated regions in Figure 6 (Imanishi & Nakanishi 2014). If this is the case, sufficient excitation at up to J=4 in IRAS 20551–4250 contributes to its higher HCN-to-HCO⁺ flux ratio at J=4–3 (and J=3–2) than starburst-dominated regions.

4.2. Vibrationally excited HCN/HCO⁺/HNC J=3–2 emission lines

HCN, HCO⁺, and HNC have three vibrational modes (v_1 , v_2 , and v_3). Since the energy level of $v_2=1$ is the lowest, its vibrational excitation is the simplest (Townes & Schawlow 1975; Amano 1983; Foster & McKellar 1984; Foster et al. 1984; Davies et al. 1984; Kawaguchi et al. 1985). HCN $v_2=1$ J=4–3 and J=3–2, and HNC $v_2=1$ J=3–2 emission lines have previously been detected in the LIRG, NGC 4418 ($L_{\text{IR}} \sim 10^{11} L_{\odot}$) (Sakamoto et al. 2010; Costagliola et al. 2013, 2015), which has observational signatures of a luminous buried AGN (Spoon et al. 2001; Evans et al. 2003; Imanishi et al. 2004; Sakamoto et al. 2013). The HCN $v_2=1$ J=4–3 emission line has also been detected in the AGN-hosting ULIRG, IRAS 20551–4250 ($L_{\text{IR}} \sim 10^{12} L_{\odot}$) (Imanishi & Nakanishi 2013b). The other AGN-hosting ULIRG, Mrk 231 ($L_{\text{IR}} \sim 10^{12.5} L_{\odot}$; Sanders et al. 2003), also shows a detectable HCN $v_2=1$ J=3–2 emission line (Aalto et al. 2015a). Very recently, the detection of HCN $v_2=1$ J=3–2 emission lines in three LIRGs (IC 860, Zw 049.057, and Arp 220) and HCN $v_2=1$ J=4–3 emission lines in two LIRGs (Arp 220W and IRAS 17208–0014) has been reported (Aalto et al. 2015b; Martin et al. 2016). This paper adds the detection of HCN $v_2=1$ J=3–2 and HNC $v_2=1$ J=3–2 emission lines in IRAS 20551–4250.

Regarding the HCO⁺ $v_2=1$ J=3–2 emission line, we obtain non-detection in our ALMA data for IRAS 20551–4250 (Table 3). The HCO⁺ $v_2=1$ emission line has never been discussed in detail for external galaxies in the published literature. Sakamoto et al. (2010) covered this HCO⁺ $v_2=1$ J=3–2 emission line in the data of NGC 4418 and reported its non-detection, with no upper limit flux provided. In the present paper, we provide the first stringent constraint on the upper limit of its flux in external galaxies.

In the case of optically thin conditions, the column density of the level u (N_u) is written as

$$N_u = \frac{4\pi}{hcA_{ul}\Omega} \times \text{flux} \quad (1)$$

$$\propto \frac{\text{flux}}{A_{ul}}, \quad (2)$$

where the line flux from the upper (u) to lower (l) transition level is in units of [Jy km s^{-1}], h is the Planck constant, c is the speed of light, Ω is the source solid angle, and A_{ul} is the Einstein A coefficient for spontaneous emission from the upper (u) to lower (l) level (Goldsmith & Langer 1999; Izumi et al. 2013). We assume that HCN, HCO⁺, and HNC surround energy sources (buried AGN and stars) with almost full covering factor in the same geometry, because (a) the optical spectroscopic non-Seyfert classification of IRAS 20551–4250 (Duc et al. 1997; Yuan et al. 2010) suggests that the putative AGN detected in

infrared and X-ray observations (§1) is obscured by dust and molecular gas in virtually all directions (=buried), and (b) newly formed stars are also deeply embedded in dust and molecular gas. Namely, emission structure inside the ALMA synthesized beam is assumed to be the same among HCN, HCO⁺, and HNC. Adopting the Einstein A coefficients from the J=3 to J=2 level at $v_2=1$ shown in Table 5, the ratio of the column density at the $v_2=1$ J=3 level among HCN, HCO⁺, and HNC is

$$\text{HCN} : \text{HCO}^+ : \text{HNC} (N_{v_2=1, J=3}) (\text{observed}) = 1 : < 0.20 : 0.69, \quad (3)$$

where the fluxes based on Gaussian fits (Table 3, column 10) are used for the detected HCN $v_2=1$ J=3–2 and HNC $v_2=1$ J=3–2 lines, whereas the upper limit ($<3\sigma$) in the integrated intensity (moment 0) map (Table 3, column 3) is adopted for the undetected HCO⁺ $v_2=1$ J=3–2 line. This will be compared to theoretical calculations in the following subsection. If HC₃N $v_7=1$ J=30–29 emission blends with HNC $v_2=1$ J=3–2 (Costagliola et al. 2013), the actual HNC $v_2=1$ J=3–2 emission line flux could be smaller by 25–50% (Table 3).

The ratios of observed $v_2=1$ J=3–2 to $v=0$ J=3–2 flux in units of [Jy km s^{-1}] for HCN, HCO⁺, and HNC are summarized in Table 6. The ratios are

$$\text{HCN} : \text{HCO}^+ : \text{HNC} (v_2 = 1f/v = 0) (\text{observed}) = 1 : < 0.25 : 1.4, \quad (4)$$

This is the second observed quantity to indicate the efficiency of vibrational excitation to the $v_2=1$ level.

4.3. Comparison with infrared radiative pumping model

4.3.1. Abundance ratio among HCN, HCO⁺, and HNC

The energy levels of $v_2=1$ are ~ 1030 K (HCN), ~ 1200 K (HCO⁺), and ~ 670 K (HNC). These energy levels are too high to be collisionally excited, but could be excited by infrared radiative pumping, by absorbing infrared photons at $\sim 14 \mu\text{m}$ (HCN), $\sim 12 \mu\text{m}$ (HCO⁺), and $\sim 21.5 \mu\text{m}$ (HNC). The ratio in Equation (3) reflects the product of the infrared radiative pumping rate to $v_2=1$ and column density at $v=0$ of each molecule. To estimate the effect of the infrared radiative pumping, we assume that (a) HCN, HCO⁺, and HNC emission lines at both $v=0$ and $v_2=1$ come from the same regions, relative to the central buried AGN of IRAS 20551–4250, and (b) the column density at $v=0$ ($N_{v=0}$) is comparable among HCN, HCO⁺, and HNC. The first assumption comes from the fact that HCN, HCO⁺, and HNC have similar dipole moments ($\mu = 3.0, 3.9$, and 3.1 Debye, respectively), and so their emission lines at the same J-transition at $v=0$ probe similarly dense molecular gas in a galaxy, compared to the widely-used CO J-lines ($\mu = 0.1$ Debye), which trace much less dense molecular gas at the same J-transition. Here, it is assumed that $v_2=1$ emission also comes from the same regions. These assumptions will be discussed later.

The infrared radiative pumping rate (P_{IR}) is

$$P_{\text{IR}} \propto B_{v_2=0-1, vib} \times F_{\nu(\text{IR})} \times N_{v=0}, \quad (5)$$

where $B_{v_2=0-1, vib}$ is the Einstein B coefficient from $v=0$ to $v_2=1$, $F_{\nu(\text{IR})}$ is infrared flux in F_{ν} [Jy] used for the infrared radiative pumping of HCN/HCO⁺/HNC, and $N_{v=0}$ is the column density at the $v=0$ level. The $B_{v_2=0-1, vib}$ is related to the Einstein A coefficient from $v_2=1$ to $v=0$ ($A_{v_2=1-0, vib}$) in the form of

$$B_{v_2=0-1, vib} \propto \lambda^3 \times A_{v_2=1-0, vib} \quad (6)$$

(Rybicki & Lightman 1979).

For $v_2=1$, the $A_{v_2=1-0,vib}$ values are estimated to be $\sim 1.7 \text{ s}^{-1}$ (HCN) (Deguchi et al. 1986; Aalto et al. 2007), $\sim 3.0 \text{ s}^{-1}$ (HCO^+) (Mauclaire et al. 1995), and $\sim 5.2 \text{ s}^{-1}$ (HNC) (Aalto et al. 2007). Thus, the ratio of the $B_{v_2=0-1,vib}$ value among HCN, HCO^+ , and HNC is

$$\text{HCN} : \text{HCO}^+ : \text{HNC}(B_{v_2=0-1,vib}) = 1 : 1.1 : 11 \quad (7)$$

The infrared flux for the infrared radiative pumping of HCN ($14 \mu\text{m}$), HCO^+ ($12 \mu\text{m}$), and HNC ($21.5 \mu\text{m}$) is estimated from the $5\text{--}35 \mu\text{m}$ spectrum of IRAS 20551–4250 taken by Spitzer IRS (Fig. 7). The $5\text{--}35 \mu\text{m}$ spectrum in Figure 7 shows strong silicate dust absorption features at $\lambda_{\text{rest}} \sim 9.7 \mu\text{m}$ and $18 \mu\text{m}$ (rest-frame), which means that mid-infrared ($3\text{--}20 \mu\text{m}$) continuum emission originated in energy sources (buried AGN and/or stars) is obscured by dust at the foreground. We need to correct for these silicate dust absorption features, if we are to obtain the intrinsic mid-infrared spectral energy distribution which is produced in the close vicinity of the obscured energy sources and is illuminated to their nearby molecular gas.

The HCN $v_2=1f$ $J=3\text{--}2$ or $J=4\text{--}3$ emission was detected in some Galactic sources (Ziurys & Turner 1986; Mills et al. 2013; Veach et al. 2013; Nagy et al. 2015). Since the emission can be produced in the region where infrared $14 \mu\text{m}$ photons are available and since Galactic sources emit some amount of infrared $14 \mu\text{m}$ photons, the detection in nearby Galactic sources is reasonable, as long as observations are sensitive enough to detect low luminosity emission. However, IRAS 20551–4250 at $z=0.043$ (luminosity distance is 188 Mpc) is much further away from our Galaxy and the detected $v_2=1f$ emission line luminosity in IRAS 20551–4250 (Table 4) is more than several orders of magnitude higher than the Galactic sources. Since an AGN is a much stronger mid-infrared continuum emitter than a starburst under the same bolometric luminosity, due to the larger amount of hot dust in the former (§1), an AGN can produce strong $v_2=1f$ emission more easily than stars. Nardini et al. (2008, 2009) estimated that $\sim 90\%$ of the observed $5\text{--}8 \mu\text{m}$ flux of IRAS 20551–4250 comes from AGN-heated hot dust emission. We also investigate the rest-frame equivalent widths of the $6.2 \mu\text{m}$, $7.7 \mu\text{m}$, and $11.3 \mu\text{m}$ polycyclic aromatic hydrocarbon (PAH) emission features from the spectrum of IRAS 20551–4250 in Figure 7, using the same definition as that employed by Imanishi et al. (2007b). It is widely accepted that a starburst shows strong PAH emission features, while a pure AGN does not (Moorwood 1986; Genzel et al. 1998; Imanishi & Dudley 2000), because PAHs are destroyed in the close vicinity of an AGN (Voit 1992). The derived rest-frame equivalent widths of the $6.2 \mu\text{m}$, $7.7 \mu\text{m}$, and $11.3 \mu\text{m}$ PAH emission features are ~ 45 [nm], ~ 190 [nm], and ~ 185 [nm], respectively. These values are much smaller than the typical values found in starburst-dominated galaxies (~ 540 [nm], ~ 690 [nm], and ~ 600 [nm] for the $6.2 \mu\text{m}$, $7.7 \mu\text{m}$, and $11.3 \mu\text{m}$ PAH emission features, respectively) (Imanishi et al. 2007b), which again supports the scenario that the observed mid-infrared flux of this galaxy is dominated by AGN-heated hot dust emission. Farrah et al. (2003) also modeled that the observed $10\text{--}25 \mu\text{m}$ emission of IRAS 20551–4250 is dominated by an AGN-origin dust continuum emission com-

ponent. Thus, we regard that the observed mid-infrared continuum from IRAS 20551–4250 is dominated by the AGN-heated hot dust emission. Since the AGN-heated hot dust emission is spatially very compact and is more centrally-concentrated than surrounding dust (Imanishi et al. 2007b), a simple foreground screen dust model is applicable.

Following Imanishi et al. (2007b), we adopt power-law-shaped intrinsic continua, using data unaffected by the silicate dust absorption features and strong PAH emission features. The derived intrinsic power law continua, after correcting for the silicate dust absorption features using the foreground screen dust model, are shown in Figure 7. The ratio of the infrared flux used for the infrared radiative pumping among HCN ($14 \mu\text{m}$), HCO^+ ($12 \mu\text{m}$), and HNC ($21.5 \mu\text{m}$) is

$$\text{HCN} : \text{HCO}^+ : \text{HNC}(F_{\nu(IR)}) = 1 : 0.8 : 2.5, \quad (8)$$

where we compare the power-law continuum fluxes at the redshifted wavelengths with $z = 0.043$. The infrared spectral energy distribution of the hidden energy source of IRAS 20551–4250 (in F_{ν}) shows higher fluxes with increasing wavelength at $5\text{--}35 \mu\text{m}$. Strictly speaking, the continuum emission, outside the strong silicate dust absorption features, could be flux-attenuated by foreground dust absorption, and its shape could change slightly. However, as we will show below, this change is insignificant. The optical depth of the $9.7 \mu\text{m}$ silicate dust absorption feature, relative to the adopted power law continuum level in Figure 7, is estimated to be $\tau_{9.7} \sim 2.7$. This corresponds to $A_V = 25\text{--}50$ mag, if the relation of $\tau_{9.7}/A_V = 0.054\text{--}0.11$, found in the Galactic interstellar medium (Roche & Aitken 1984, 1985), is adopted. The dust extinction at $5\text{--}20 \mu\text{m}$, outside the strong silicate dust absorption features (A_{MIR}), is $A_{\text{MIR}} = 0.027 \times A_V$ (Nishiyama et al. 2008, 2009), or $A_{\text{MIR}} = 0.7\text{--}1.4$ mag in the case of IRAS 20551–4250. Since the dust extinction curve at $5\text{--}20 \mu\text{m}$ is relatively flat (Fritz et al. 2011), the possible change in the intrinsic continuum spectral shape at $5\text{--}20 \mu\text{m}$ outside the silicate dust absorption features, through dust extinction, is too small to significantly affect our discussion. Thus, we adopt the ratio of Equation (8).

Adopting the above values, the ratio of the infrared radiative pumping rate among HCN, HCO^+ , and HNC is

$$\text{HCN} : \text{HCO}^+ : \text{HNC}(P_{IR})(\text{predicted}) = 1 : 0.9 : 279$$

Namely, the infrared radiative pumping rate of HNC is much higher than HCN and HCO^+ , mainly due to the longer wavelength of the infrared $v_2=1$ absorption line. The Einstein A coefficient for the rotational $J=3\text{--}2$ transition at $v_2=1f$ ($A_{J=3-2,rot,v_2=1f}$), relative to that for the vibrational transition from $v_2=1$ to $v=0$ ($A_{v_2=1-0,vib}$), is $\sim 4 \times 10^{-4}$, $\sim 4 \times 10^{-4}$, and $\sim 2 \times 10^{-4}$ for HCN, HCO^+ , and HNC, respectively (Table 5 and §4.3.1, third paragraph). Thus, most of the vibrationally excited molecules to $v_2=1$ quickly decay back to $v=0$, rather than decaying to a lower rotational-J level at $v_2=1$. However, the $A_{J=3-2,rot,v_2=1f}$ to $A_{v_2=1-0,vib}$ ratios agree within a factor of ~ 2 among HCN, HCO^+ , and HNC. Once vibrationally excited to $J=3$ at $v_2=1f$, a similar fixed fraction of rotational J-transition from $J=3$ to $J=2$

at $v_2=1f$ is expected, which should be detectable as the $v_2=1f$ J=3–2 emission line. Thus, the detection of the HNC $v_2=1f$ J=3–2 emission line in a galaxy with detectable HCN $v_2=1f$ J=3–2 and J=4–3 emission lines is quite reasonable, under our current assumption that HCN and HNC have comparable column density at $v=0$. On the other hand, the radiative pumping rates of HCN and HCO⁺ are comparable. The detection of the HCN $v_2=1f$ J=3–2 emission line, without the detection of the HCO⁺ $v_2=1f$ J=3–2 emission line, requires some consideration.

When the $v_2=1$ to $v=0$ column density ratio ($N_{v_2=1}/N_{v=0}$), controlled by the infrared radiative pumping, is $\ll 1$ (see §4.5), we obtain the relation

$$N_{v=0} \times B_{v_2=0-1,vib} \times F_{\nu(IR)} = N_{v_2=1} \times A_{v_2=1-0,vib} \quad (10)$$

Here, transitions among rotational J-levels within $v=0$ and $v_2=1$ are neglected. From this equation, we obtain

$$\frac{N_{v_2=1}}{N_{v=0}} = \frac{B_{v_2=0-1,vib} \times F_{\nu(IR)}}{A_{v_2=1-0,vib}} \quad (11)$$

$$\propto \lambda^3 \times F_{\nu(IR)}, \quad (12)$$

where the relation in Equation (6) is used. Thus, the $v_2=1$ to $v=0$ column density ratios among HCN, HCO⁺, and HNC are

$$HCN : HCO^+ : HNC(N_{v_2=1}/N_{v=0})(predicted) = 1 : 0.5(13)$$

We note that Ziurys & Turner (1986) adopt a higher $A_{v_2=1-0,vib}$ value of 3.7 s^{-1} for HCN than our assumption (1.7 s^{-1}). However, this predicted column density ratio is independent of the absolute $A_{v_2=1-0,vib}$ values of HCN, HCO⁺, HNC, because of the division of $A_{v_2=1-0,vib}$ by $B_{v_2=0-1,vib}$, as shown in Equations (11) and (12). Thus, the predicted ratio is robust to the possible uncertainty of the absolute $A_{v_2=1-0,vib}$ values of HCN, HCO⁺, and HNC.

The observed J=4–3 to J=3–2 flux ratios in §4.1 suggest that HCN, HCO⁺, and HNC are almost thermally excited and so are similarly populated at J=3 and J=4 at $v=0$. Assuming that the fraction of J=3 level, relative to all J-levels at $v=0$, is similar among HCN, HCO⁺, and HNC, Equations (3) (observation) and (13) (prediction) can be compared if the column density at $v=0$ (and thereby abundance, which is proportional to the column density) is the same among HCN, HCO⁺, and HNC. The discrepancy between observation (Eqn. (3)) and prediction (Eqn. (13)) can be reconciled if the column density at $v=0$ ($N_{v=0}$) for HCN is higher than HCO⁺ and HNC by factors of >2.5 and 13, respectively, where HCN/HCO⁺/HNC $v_2=1f$ J-transition emission is assumed to be optically thin. Namely, the HCN-to-HCO⁺ abundance ratio of >2.5 and HCN-to-HNC abundance ratio of 13 are suggested for the IRAS 20551–4250 nucleus. The HCN-to-HNC abundance ratio could be even higher if the HNC $v_2=1f$ J=3–2 emission line flux is contaminated by HC₃N $v_7 = 1f$ J=30–29 line (Table 3). In summary, we obtain the abundance ratio of

$$HCN : HCO^+ : HNC(abundance) = 1 : < 0.4 : < 0.08 \quad (14)$$

The higher abundance (and thereby higher column density at $v=0$) of HCN than HCO⁺ and HNC, derived in Equation (14), can naturally explain the following observational results that (a) HCN $v_2=1f$ J=3–2 emission line

is detected, without HCO⁺ $v_2=1f$ J=3–2 emission line detection, despite the similar infrared radiative pumping rate to the $v_2=1$ level (Eqn. (9)), and (b) the $v_2=1f$ J=3–2 emission line fluxes are similar between HCN and HNC (Table 5), despite the much higher predicted infrared radiative pumping rate to $v_2=1$ in HNC than HCN (Eqn. (9)). Given that the bulk of the mid-infrared photons used for the vibrational excitation of HCN/HCO⁺/HNC is interpreted to originate from AGN-heated hot dust thermal radiation, the properties of molecular gas derived from the $v_2=1f$ emission lines (i.e., higher abundance of HCN than HCO⁺ and HNC) should reflect those of AGN-affected molecular gas in the close vicinity of an AGN.

In our Milky Way Galaxy, the HCN-to-HCO⁺ abundance ratio is estimated to be 1.2 ± 0.4 in infrared dark clouds, based on molecular emission line studies (Liu et al. 2013) and 1.9 ± 0.9 in diffuse interstellar medium, based on molecular absorption line studies (Godard et al. 2010). However, it has been suggested from observations and their interpretations that the HCN-to-HCO⁺ abundance ratio is high in molecular gas in the close vicinity of AGNs (Yamada et al. 2007; Izumi et al. 2016). Thus, the derived HCN-to-HCO⁺ abundance ratio with >2.5 at the IRAS 20551–4250 nucleus would be possible.

With respect to HCN and HNC, in our Galaxy, the abundance of HCN and HNC are comparable in cold dark clouds (Liu et al. 2013; Hirota et al. 1998; Graninger et al. 2014). However, in high temperature clouds around active regions, the HNC abundance decreases by more than an order of magnitude, relative to the HCN abundance (Schilke et al. 1992; Hirota et al. 1998; Graninger et al. 2014). Given that the bulk of HCN and HNC J=3–2 emission at $v_2=1$ and $v=0$ detected in the ALMA data for IRAS 20551–4250 come from nuclear active regions (§3), the increase in the HCN-to-HNC abundance ratio by more than an order of magnitude could occur.

Summarizing, our results suggest that in the nuclear region of IRAS 20551–4250, the HCN-to-HCO⁺ and HCN-to-HNC abundance ratios are >2.5 and >10 , respectively, which is quite possible based on previously obtained observational data from our own Galaxy and other galaxies.

The HCN $v_2=1f$ J=3–2 or J=4–3 emission lines were detected in some Galactic objects and star-forming regions, despite much lower luminosity than IRAS 20551–4250 (Ziurys & Turner 1986; Veatch et al. 2013; Mills et al. 2013; Nagy et al. 2015). However, the relative strengths of HCO⁺ and HNC $v_2=1f$ J=3–2 or J=4–3 emission lines are not known, except for the luminous active star-forming region W49A, in which the $v_2=1f$ J=4–3 emission line was detected for HCN and HNC, but not for HCO⁺ with no flux upper limit provided (Nagy et al. 2015). Infrared 5–14.5 μm spectra were taken at some offset regions in the vicinity of the W49A center (Stock et al. 2014), but are not available at the W49A center, where the $v_2=1f$ J=4–3 emission lines of HCN and HNC are detected (Nagy et al. 2015). Thus, the same analysis to derive molecular abundance ratios as made for IRAS 20551–4250 in the earlier part of this section is currently not applicable to the W49A center and other Galactic sources with detectable HCN $v_2=1f$ emission lines. It might be possible that some specific Galactic stellar populations show an enhanced HCN abundance

in their vicinity, despite the fact that a modest HCN-to-HCO⁺ abundance ratio ($=1.9\pm0.9$) is derived, based on absorption studies of Galactic sources (Godard et al. 2010), which probe the ratio in a larger Galactic physical scale, in front of the background continuum emitting sources, than emission-based abundance measurements.

There is an observational trend that the observed HCN-to-HCO⁺ flux ratios in AGNs are higher than starburst galaxies (§1). The observed HCN-to-HCO⁺ J=4–3 flux ratio at the W49A center is also low, only ~ 0.4 (Nagy et al. 2015). High observed HCN-to-HCO⁺ flux ratios at J=4–3 or J=3–2 are produced not only by high HCN-to-HCO⁺ abundance ratios, but also by sufficient excitation to J=4 and 3, particularly for HCN, due to its higher critical density than HCO⁺ (§4.1). Since excitation to J=4 or 3 is more efficiently achieved in an AGN than star-formation, because of AGN’s much higher radiative energy generation efficiency (§1), buried AGN selection based on high HCN-to-HCO⁺ flux ratios remains effective. Since an AGN is expected to show a higher mid-infrared 14 μm to infrared (8–1000 μm) luminosity ratio than star-formation, due to AGN-heated hot dust (§1), the HCN $v_2=1\text{f}$ J=4–3 to infrared luminosity ratio in IRAS 20551–4250 is expected to be even higher than that in W49A, if IRAS 20551–4250 indeed contains a luminous buried AGN. For W49A, adopting the infrared luminosity of $>10^7 L_\odot$ and distance of 11 kpc (Nagy et al. 2015), the HCN $v_2=1\text{f}$ J=4–3 to infrared luminosity ratio is $<1.2\times 10^{-9}$. The ratio for IRAS 20551–4250 is estimated to be 4.9×10^{-9} , based on the infrared luminosity of $L_{\text{IR}} = 10^{12.0} L_\odot$ (§1) and observed HCN $v_2=1\text{f}$ J=4–3 luminosity (Table 4). This ratio is more than a factor of four higher than W49A, supporting the strong AGN contributions to molecular gas emission at the IRAS 20551–4250 nucleus.

4.3.2. Flux-attenuation of HCN/HCO⁺/HNC $v=0$ J=3–2 Emission

In Equation (4), because the Einstein A coefficient for spontaneous emission from J=3 to J=2 is almost identical between $v=0$ and $v_2=1\text{f}$ (Table 5), the ratio is roughly converted into the column density ratio at $v_2=1\text{f}$ J=3 and $v=0$ J=3 (see Eqn. (2)), provided that the opacity of $v=0$ J=3–2 emission is insignificant. In other words, the ratios in Equations (4) and (13) can be used to estimate the opacity of $v=0$ J=3–2 emission for HCN, HCO⁺, and HNC. From this comparison, we derive that the flux attenuation of HCN $v=0$ J=3–2 emission is a factor of >2 larger than that of HCO⁺ $v=0$ J=3–2 emission, and is a factor of 6 larger than that of HNC $v=0$ J=3–2 emission.

The observed HCN J=3–2 to H¹³CN J=3–2 flux ratio is ~ 16 (Table 3). The ¹²C/¹³C abundance ratios in starburst galaxies are estimated to be ~ 50 (Henkel & Mauersberger 1993; Henkel et al. 1993, 2014) or possibly even higher (Martin et al. 2010). In ULIRGs, the ¹²C/¹³C abundance ratios are as high as ~ 100 (Henkel et al. 2014). Assuming optically thin emission for H¹³CN J=3–2, HCN J=3–2 emission is estimated to be optically thick, and its flux can be attenuated by a factor of 3–6. In this case, the flux attenuation of HNC $v=0$ J=3–2 emission becomes 0.5 (if the flux attenuation of HCN $v=0$ J=3–2 emission is 3) or 1 (if that of HCN $v=0$ J=3–2 emission is 6). Since the flux attenuation factor by line opacity is by definition always larger than unity, we

adopt the flux attenuation of HCN J=3–2 emission to be 6, which provides the flux attenuation of HCO⁺ $v=0$ J=3–2 emission to be <3 .

According to the widely accepted model of molecular gas in galaxies, molecular clouds consist of clumpy structures, rather than spatially smooth distribution, because observed molecular gas properties are better explained by the former clumpy model (Solomon et al. 1979, 1987). Each clump can be optically thick, but has random motion inside molecular clouds, so that emission from clumps at the other side of molecular clouds is not significantly flux-attenuated by foreground molecular gas clumps (Solomon et al. 1987). The physical properties of individual clumps are assumed to be the same throughout a molecular cloud and among different molecular clouds. In this model, profiles of molecular lines with even different line opacity are expected to be similar. Figure 8 shows similar $v=0$ J=3–2 emission line profiles of HCN, HCO⁺, and HNC, supporting the above clumpy molecular gas model for IRAS 20551–4250.

Adopting this clumpy molecular gas model, line opacity comes mostly from the individual line emitting clumps, rather than foreground molecular gas. The flux attenuation factor is expressed by

$$\text{Flux} - \text{attenuation} = \frac{\tau}{1 - e^{-\tau}}, \quad (15)$$

where τ is an optical depth, which is proportional to column density. The flux attenuation of 6 for HCN $v=0$ J=3–2 emission corresponds to $\tau = 6$. In the same way, we obtain $\tau < 2.8$ for HCO⁺ $v=0$ J=3–2 emission. For HNC J=3–2, the flux attenuation is estimated to be not substantially larger than unity. We adopt $\tau < 1$ for HNC $v=0$ J=3–2 emission, in which case the flux attenuation is <1.6 . Consequently, we obtain the following optical depth ratio among HCN, HCO⁺, and HNC J=3–2 at $v=0$,

$$\text{HCN} : \text{HCO}^+ : \text{HNC}(\tau) = 1 : < 0.5 : < 0.2. \quad (16)$$

If the optical depth in thermally excited gas is small, the J=4–3 to J=3–2 flux ratio can be higher than that of thermally excited optically thick gas. The possibly higher J=4–3 to J=3–2 flux ratio for HNC (1.8 ± 0.2) than HCN (1.6 ± 0.2) (§4.1) might be related to the small optical depth of HNC.

The optical depth ratio among $v=0$ J=3–2 emission lines of HCN, HCO⁺, and HNC can be roughly estimated independently from the abundance ratio in Equation (14). Considering the transitions between J=3 and J=2 ($v=0$), the optical depth value is expressed as

$$\tau \propto \nu \times N_2 \times B_{J=2-3, \text{rot}} \times (1 - g_2 n_3 / g_3 n_2) \quad (17)$$

$$\propto \nu^{-2} \times N_2 \times A_{J=3-2, \text{rot}} \times (1 - g_2 n_3 / g_3 n_2) \quad (18)$$

where N_2 is the column density at J=2 ($v=0$), n_J is the number density at J=2 or J=3 ($v=0$), $B_{J=2-3, \text{rot}}$ is the Einstein B coefficient for rotational transition from J=2 to J=3 ($v=0$), $A_{J=3-2, \text{rot}}$ is the Einstein A coefficient for spontaneous emission for rotational transition from J=3 to J=2 ($v=0$), ν is frequency, and g_J is the statistical weight that is related to the J-level in the form of $2J+1$ (Rybicki & Lightman 1979). In IRAS 20551–4250, since HCN, HCO⁺, and HNC are found to be almost thermally excited at J=3 and J=4, the $g_2 n_3 / g_3 n_2$ term

is expressed with $\exp(-E/k_B T_{\text{kin}})$, where E is the energy level of the J-transition of interest, T_{kin} is the kinetic temperature of molecular gas, and k_B is the Boltzmann constant. For HCN, HCO⁺, and HNC, since energy levels and frequencies are almost the same for the same rotational J-transitions at $v=0$, the term of $\nu^{-2} \times (1-g_{2n_3}/g_{3n_2})$ is also nearly identical. Adopting the $A_{J=3-2, \text{rot}}$ values shown in Table 5, we obtain the following optical depth ratio, from the derived abundance ratio in Equation (14),

$$\text{HCN} : \text{HCO}^+ : \text{HNC}(\tau_2) = 1 : < 0.7 : < 0.1. \quad (19)$$

The two independently derived optical depth ratios in Equations (16) and (19) show consistent results to each other. The ratios of various parameters among HCN, HCO⁺, and HNC used for our discussion are summarized in Table 7.

We now correct for the flux attenuation by line opacity, to derive the intrinsic HCN-to-HCO⁺ and HCN-to-HNC flux ratios from the observed ratios in Figure 6. For J=3–2, we adopt the flux attenuation with factors of 6, <3, and ~ 1 for HCN, HCO⁺, and HNC, respectively (§4.3.2, second paragraph). For J=4–3, the observed HCN-to-HCO⁺ and HCN-to-HNC flux ratios are almost identical to those at J=3–2. Since excitation condition does not significantly change the flux ratios between J=3–2 and J=4–3 in IRAS 20551–4250 (§4.1) and since the abundance effect should be the same between J=3–2 and J=4–3, the observed flux ratios at J=4–3 can be naturally interpreted with the similar intrinsic flux ratios and flux attenuation to J=3–2. We thus apply the same flux attenuation correction for J=4–3 as employed above for J=3–2.

The intrinsic molecular line flux ratio of IRAS 20551–4250 at J=3–2 and J=4–3, after the correction for flux attenuation by line opacity, are plotted as open symbols in Figure 6, which are further deviating from the distribution of starburst-dominated regions. Other data points could also move if opacity-corrected intrinsic flux ratios are used. If HCN flux enhancement is indeed a good signature of AGNs, and if this is due in part to HCN abundance enhancement, then the line opacity of HCN emission and thereby the opacity correction factor of HCN flux, relative to HCO⁺ and HNC, could be higher in AGNs than in starburst galaxies. This will move AGNs to the right and upper direction, even deviating from the distribution of starburst galaxies. This could make the HCN-flux-based separation between AGNs and starbursts more solid. Furthermore, if higher HCN opacity is the case in AGNs, while some AGNs show enhanced observed HCN fluxes, other AGNs may not. This could explain the result that some fraction of AGNs do not necessarily show observed HCN flux enhancements (Privon et al. 2015), although it is possible that the result is partly due to the dilution of the signatures of AGN-affected molecular gas emission, by the large contamination from spatially-extended starburst-affected molecular gas emission in their large-aperture single-dish telescope data. Correction for flux attenuation through isotopologue observations (e.g., H¹³CN, H¹³CO⁺, HN¹³C, HC¹⁵N, H¹⁵NC) is necessary not only for IRAS 20551–4250, but also for other galaxies, to derive intrinsic flux ratios in Figure 6.

Finally, in Figure 6, IRAS 22491–1808 shows no

clear infrared-identified buried AGN signatures, and yet shows a high HCN-to-HCO⁺ flux ratio at J=4–3 (Imanishi & Nakanishi 2013b). For IRAS 22491–1808, the HCN $v_2=1f$ J=3–2 emission line has been detected in our ALMA Cycle 2 data (Imanishi et al. 2016), suggesting the presence of a strongly 14 μm emitting energy source, which is naturally explained by a luminous buried AGN, due to AGN-heated hot dust (§1 and §4.3.1). IRAS 22491–1808 may contain an extremely deeply buried AGN whose signatures are not detectable in infrared energy diagnostic methods, but can be detected in (sub)millimeter observations for the first time, due to reduced effects of dust extinction. The presence of similar sources, infrared-classified-starbursts with elevated HCN-to-HCO⁺ flux ratios, is found also at J=1–0 (Costagliola et al. 2011; Privon et al. 2015). ALMA (sub)millimeter observations of these sources are interesting to scrutinize the presence of infrared-elusive, but (sub)millimeter-detectable, extremely deeply buried AGNs.

4.4. Possible caveats

We here comment a few caveats for our discussion above. First, transitions among rotational J-levels within $v=0$ and $v_2=1$ are not treated in our calculations (Eqns. (10)–(12)), because the number of currently available molecular J-transition data is not large enough to do this in a reliable manner. This could be the largest uncertainty. However, the similar excitation up to J=4 at $v=0$ among HCN, HCO⁺, and HNC, estimated from their similar observed J=4–3 to J=3–2 flux ratios (§4.1), suggests that the effects of this uncertainty for our discussion at J=3 and J=4 are expected to be relatively limited, unless excitation at higher-J is considerably different among HCN, HCO⁺, and HNC. When more J-transition data become available, this point will be tested more.

Second, we assumed that HCN, HCO⁺, and HNC emission both at $v=0$ and $v_2=1$ come from the same region (§4.3.1). This is clearly too simplistic. Even though the dipole moments are comparable among HCN, HCO⁺, and HNC (§4.3.1), their critical densities are not perfectly the same. HCO⁺ has a lower critical density than HCN and HNC by a factor of ~ 5 for the same J-transition at $v=0$ (Meijerink et al. 2007; Greve et al. 2009), so that the spatial extent of collisionally-excited HCO⁺ $v=0$ J=3–2 emission line can be larger than those of HCN/HNC $v=0$ J=3–2 emission lines, if molecular gas has a gradually decreasing radial density distribution from the very center to the outer region in a galaxy (Bigiel & Blitz 2012), due to the decrease of typical density of individual molecular gas clumps. In fact, it is sometimes seen in a galaxy nuclear scale that HCO⁺ emission is spatially more extended than HCN emission at the same J-transition (Imanishi et al. 2007a; Saito et al. 2015). This is also the case for IRAS 20551–4250, because HCO⁺ $v=0$ J=3–2 emission is estimated to be slightly more extended spatially than HCN/HNC $v=0$ J=3–2 emission (§3). The size of the continuum emitting region around a buried AGN is also different at 14 μm (used for the vibrational excitation to $v_2=1$ for HCN), 12 μm (HCO⁺), and 21.5 μm (HNC). These different geometries are shown as schematic diagrams in Figure 9. For the $v_2=1f$ J=3–2 emission, in the case of constant radial density distribution of molecular gas, since

the number of infrared photons per molecule is larger in the close vicinity of an AGN than the outer part, the $v_2=1f$ to $v=0$ flux ratios of HCN/HCO⁺/HNC should be higher at the inner part, and the bulk of the $v_2=1f$ J=3–2 emission is likely to come from the inner region in Figure 9. Emission-weighted size of the $v_2=1f$ J=3–2 line can become smaller than that of the $v=0$ J=3–2 line for HCN/HCO⁺/HNC. The difference of $v_2=1f$ to $v=0$ flux ratios between the inner and outer parts, and the emission-weighted size difference between $v_2=1f$ and $v=0$, are reduced, if molecular gas has a decreasing radial density distribution from the galaxy center to the outer part. We need to consider how these differences in geometry could alter our results obtained based on the assumption that HCN/HCO⁺/HNC $v=0$ and $v_2=1f$ lines come from the same volume.

Regarding the size difference between $v_2=1f$ J=3–2 and $v=0$ J=3–2 emission, the total fluxes of HCN/HCO⁺/HNC $v_2=1f$ J=3–2 emission lines from molecular gas in Figure 9 are primarily determined by the number of infrared photons which are absorbed and used for the vibrational excitation to $v_2=1$. As long as (a) the covering solid angle around the central infrared continuum emitting energy source does not differ a lot among HCN, HCO⁺, and HNC, and (b) the bulk of the $v_2=1f$ J=3–2 emission is covered within our ALMA beam, then our discussion in §4.3 is essentially unchanged. Both of the conditions (a) and (b) are likely to be met.

Regarding the size difference of the infrared continuum emitting regions among HCN/HCO⁺/HNC, the most important factor for our infrared radiative pumping calculations of $v_2=1f$ fluxes in §4.3.1 is again the number of infrared photons used for the vibrational excitation to $v_2=1$. The slight difference of the spatial extent of continuum emitting regions at different infrared wavelengths will not alter our results significantly, as long as (a) the infrared continuum emitting regions are more compact than the surrounding molecular gas, and (b) the covering fraction around the central energy source is similar among HCN, HCO⁺, and HNC. Both of the conditions (a) and (b) are expected to be fulfilled.

Regarding the size difference of $v=0$ J=3–2 emission among HCN, HCO⁺, and HNC, the HCO⁺ J=3–2 emission is estimated to be spatially more extended than HCN/HNC J=3–2 emission inside the ALMA beam (§3). In this case, the source solid angle (Ω) in Equation (1) becomes larger for HCO⁺ J=3–2 than HCN/HNC J=3–2, and the HCO⁺ J=3–2 ($v=0$) column density is smaller than our estimate. This affects our discussion of column density and thereby abundance. In fact, if both HCN J=3–2 and HCO⁺ J=3–2 emission are thermalized (excitation temperature is comparable to the kinetic temperature of molecular gas) (§4.1) and if the optical depth of HCN J=3–2 line is larger than that of HCO⁺ J=3–2 line (§4.3.2), then the HCO⁺ J=3–2 flux cannot be larger than the HCN J=3–2 flux, as long as both lines are emitted from the same volume, because their frequencies are almost identical. The HCO⁺ $v=0$ J=3–2 to HCN $v=0$ J=3–2 flux ratio of 1.4 (Table 5) can be explained, if the HCO⁺ $v=0$ J=3–2 line emitting region is >1.4 times larger in Ω than the HCN J=3–2 line emitting region within our ALMA beam. In our ALMA data, the spatial extent of HCO⁺ $v=0$ J=3–2 emission is estimated to be larger than those of HCN/HNC $v=0$ J=3–2 emission

by a factor of ~ 1.5 in Ω (§3). In this case, the actual HCO⁺ column density (abundance) relative to HCN will decrease by $\sim 50\%$. This will even strengthen our result that HCN-to-HCO⁺ abundance ratio is high in the IRAS 20551–4250 nucleus. It is also possible that due to the lower critical density of HCO⁺ $v=0$ J=3–2 than HCN/HNC $v=0$ J=3–2, the size of individual molecular gas clumps is larger for HCO⁺ $v=0$ J=3–2 than HCN/HNC $v=0$ J=3–2, if each molecular clump has a decreasing radial density distribution (Gierens et al. 1992; Imanishi et al. 2007a). In this case, HCO⁺ $v=0$ J=3–2 emission could occupy a larger volume fraction inside a molecular cloud than HCN/HNC $v=0$ J=3–2 emission. This will also work to decrease the HCO⁺ column density (abundance) relative to HCN and HNC, which again reinforces our main result of enhanced HCN-to-HCO⁺ abundance ratio in the nucleus of IRAS 20551–4250.

Third, we assumed that the observed mid-infrared continuum is dominated by AGN-heated hot dust emission (§4.3.1). Even though this is the case for IRAS 20551–4250, there may be non-negligible contribution from starburst emission to the observed mid-infrared flux. Since starburst-heated dust usually has cooler temperature than AGN-heated dust, the starburst contribution to the observed mid-infrared flux becomes relatively higher at a longer wavelength (Farrah et al. 2002, 2003; Prouton et al. 2004; Vega et al. 2008; Ruiz et al. 2010). The relative contribution from starbursts can be larger at $21.5 \mu\text{m}$ (for HNC) than $12 \mu\text{m}$ (HCO⁺) and $14 \mu\text{m}$ (HCN). If certain fraction of infrared $21.5 \mu\text{m}$ flux comes from starbursts, rather than the buried AGN, the AGN-origin HNC term in Equation (13) will decrease. Even if this slightly modifies the HNC term in Equation (13), our main result of very high HCN-to-HNC abundance ratio (§4.3.1) will not change.

Summarizing, even though neglecting the transitions among rotational J-levels within $v=0$ and $v_2=1$ needs to be tested in future data, our main result is robust to possible ambiguity of the assumed geometry of HCN, HCO⁺, and HNC emission regions around energy sources.

4.5. Role of infrared radiative pumping

The excitation temperature (T_{ex}) is related to the column density at level u (N_u), in the form of

$$N_u = \frac{N_{\text{mol}}}{Q(T)} g_u \exp\left(-\frac{E_u}{k_B T_{\text{ex}}}\right), \quad (20)$$

where N_{mol} is the total column density of a given molecule, $Q(T)$ is a partition function, E_u is an energy at level u above the ground state, k_B is the Boltzmann constant, and g_u is the statistical weight. The excitation temperatures (T_{ex}) in IRAS 20551–4250, based on the observed fluxes in this paper and Imanishi & Nakanishi (2013b), are shown in Table 8. If $v_2=1$ emission is optically thin and $v=0$ emission is optically thick, the intrinsic vibrational excitation temperature ($T_{\text{ex-vib}}$) after correction for line opacity will be smaller than that based on the observed flux ratio between $v_2=1$ and $v=0$. For HCN, the $T_{\text{ex-vib}}$ values corrected for the flux attenuation with the factor of 6 for HCN $v=0$ J=3–2 emission (§4.3.2) are also shown in Table 8. The same opacity correction is applied for HCN $v=0$ J=4–3 emission (see §4.3.2).

In Table 6, we also show the HCN $v_2=1f$ to $v=0$ flux ratios at J=4–3 and/or J=3–2 in NGC 4418 and Mrk 231, for which flux attenuation of $v=0$ emission is quantitatively estimated (Sakamoto et al. 2010; Aalto et al. 2015a). The observed ratios are similar between IRAS 20551–4250 and Mrk 231. For NGC 4418, the observed HCN $v_2=1f$ to $v=0$ flux ratios at J=3–2 and J=4–3 are higher by a factor of 4–5 than IRAS 20551–4250 and Mrk 231. However, Sakamoto et al. (2010) estimated a factor of ~ 20 flux attenuation of HCN $v=0$ J=4–3 emission in NGC 4418. If we apply this correction, the intrinsic HCN $v_2=1f$ to $v=0$ flux ratios for NGC 4418 become ~ 0.01 at J=3–2 and J=4–3. For HCN emission from IRAS 20551–4250, assuming flux attenuation by a factor of 6 (see §4.3.2), the intrinsic HCN $v_2=1f$ to $v=0$ flux ratios at J=3–2 and J=4–3 become ~ 0.01 . For Mrk 231, if we adopt a factor of ~ 10 flux attenuation of HCN $v=0$ J=3–2 emission (Aalto et al. 2015a), the intrinsic HCN $v_2=1f$ to $v=0$ flux ratio at J=3–2 becomes ~ 0.005 . Given the almost identical Einstein A coefficient at $v_2=1f$ and $v=0$ for the same J transition lines (Table 5), we can derive that the population ($\propto \text{flux}/A$) at $v_2=1$ (J=3,4) is approximately 0.5–1% of that at $v=0$ (J=3,4) in IRAS 20551–4250, NGC 4418, and Mrk 231. The observed HCN $v_2=1f$ to $v=0$ flux ratios at J=4–3 or J=3–2 shown by Aalto et al. (2015b) range from ~ 0.1 (Zw 049.057 and IRAS 17208–0014) to ~ 0.2 (IC 860 and Arp 220W). The information of flux attenuation for $v=0$ emission is needed to derive the intrinsic ratio. These four sources are not included in our quantitative discussion about intrinsic flux ratios, but it is quite possible that these sources have similarly low intrinsic values to the above three LIRGs, because large line opacities for the $v=0$ emission are argued (Aalto et al. 2015b; Martin et al. 2016).

Although the HCN population at $v_2=1$ is only $\sim 1\%$ of that at $v=0$ for the same J-level, the Einstein A coefficient from $v_2=1f$ J=4 to $v=0$ J=3 ($1.7\text{--}3.7\text{ s}^{-1}$) (Deguchi et al. 1986; Ziurys & Turner 1986; Aalto et al. 2007) is nearly three orders of magnitude larger than that from $v=0$ J=4 to $v=0$ J=3 (0.002 s^{-1} ; Table 5). The photon number of the transition from $v_2=1f$ J=4 to $v=0$ J=3 is estimated to be an order of magnitude higher than that from $v=0$ J=4 to $v=0$ J=3. Therefore, we can conclude that infrared radiative pumping affects rotational excitation at $v=0$, and thus could alter the $v=0$ J-transition flux ratios compared to collisional excitation alone as the excitation mechanism.

The condition where infrared radiative pumping can have a significant influence on the HCN rotational excitation at $v=0$ is defined as

$$T_{ex-vib} > \frac{T_0}{\ln \frac{A_{v_2=1-0,vib}}{A_{rot}}}, \quad (21)$$

where T_{ex-vib} is the $v_2=1$ vibrational excitation temperature, T_0 is the energy level of HCN $v_2=1f$ J=4 or J=3, $A_{v_2=1-0,vib}$ is the Einstein A coefficient from $v_2=1$ to $v=0$, and A_{rot} is the Einstein A coefficient between J-levels at $v=0$ (Carroll & Goldsmith 1981; Sakamoto et al. 2010; Mills et al. 2013). For J=3–2, adopting $T_0=1050.0$ [K] (Table 5), $A_{v_2=1-0,vib} = 1.7\text{ s}^{-1}$ (§4.3.1), and $A_{3-2,rot} = 8.4 \times 10^{-4}$ (Table 5), the right-hand column becomes ~ 140 [K]. For J=4–3, adopting $T_0=1067.1$ [K] (Table 5), $A_{v_2=1-0,vib} = 1.7\text{ s}^{-1}$ (§4.3.1),

and $A_{4-3,rot} = 20.6 \times 10^{-4}$ (Table 5), the right-hand column becomes ~ 160 [K]. The T_{ex-vib} in the left-hand column is >275 [K], if we neglect line opacity for HCN $v=0$ emission (Table 8). Even if flux attenuation by a factor of 6 for HCN $v=0$ emission is included, the T_{ex-vib} value is still >185 [K] (Table 8). Thus, the condition in Equation (21) is fulfilled for HCN at J=4 and 3 in IRAS 20551–4250.

For HNC J=3–2, the same logic is applicable. The value in the right-hand column is 80 [K] for HNC J=3–2. However, the T_{ex-vib} value in the left-hand column is 250 [K], where the observed $v_2=1f$ and $v=0$ fluxes are used, because the flux attenuation of HNC $v=0$ J=3–2 emission is estimated to be not significantly larger than unity (§4.3.2). We can therefore conclude that infrared radiative pumping affects the HNC rotational excitation at $v=0$ as well.

For HCO⁺ J=3–2, the values in the left-hand and right-hand columns are <270 [K] and 160 [K], respectively, where the observed $v_2=1f$ and $v=0$ fluxes are used, because the estimated flux attenuation for HCO⁺ $v=0$ J=3–2 emission is <3 (§4.3.2). Although the HCO⁺ $v_2=1f$ J=3–2 flux is an upper limit, if the actual flux is larger than 5% of the upper limit, the left-hand column will be higher than the right-hand column, and thus it is still possible that infrared radiative pumping plays some role for HCO⁺.

If infrared radiative pumping is at work to excite HCN/HCO⁺/HNC molecules to the $v_2=1$ level, a sufficient number of infrared photons have to be absorbed. Figure 10 displays the Spitzer IRS high-resolution ($R \sim 600$) spectra of IRAS 20551–4250 at $\lambda_{rest} \sim 14\text{ }\mu\text{m}$ (corresponding to HCN $v_2=1$ absorption), $12\text{ }\mu\text{m}$ (HCO⁺), and $21.5\text{ }\mu\text{m}$ (HNC) (Lebouteiller et al. 2015). Although possible signatures relating to the HCN $v_2=1$ absorption features may be present, the absorption features are not clear at the expected wavelengths of HCO⁺ and HNC $v_2=1$ absorption. Assuming that HCN/HCO⁺/HNC $v_2=1$ absorption features in the infrared spectra have the same velocity profile as the HCN/HCO⁺/HNC $v_2=1f$ J=3–2 emission features at 1 mm (~ 270 GHz), the required condition for infrared radiative pumping to work is

$$\sum_{i=P,Q,R} f_i S_{IR} / \lambda_{IR} > S_{rot} / \lambda_{rot} \quad (22)$$

(Sakamoto et al. 2010). Here, S_{IR} is the continuum flux density (in [Jy]) around the absorption wavelength λ_{IR} , f_i is the fractional absorption depth at the absorption peak, and S_{rot} is the peak flux density (in [Jy]) of the $v_2=1f$ J-transition line emission at the wavelength λ_{rot} . The “ $1/\lambda$ ” term is included, because a unit frequency width for the given same velocity width, $\Delta\nu$, is inversely proportional to λ (= proportional to ν). In the left-hand term, infrared absorption by the P, Q, and R branches is summed. For HCN absorption at $\lambda_{rest} \sim 14.0\text{ }\mu\text{m}$, the absorption dip, $f_i S_{IR}$, is at most <0.03 [Jy] in the infrared spectrum (Fig. 10). The peak flux of the HCN $v_2=1f$ J=3–2 emission line in the millimeter wavelength is ~ 1.5 [mJy] (Fig. 4). The upper limit in the left-hand term of Equation (22) is approximately three orders of magnitude larger than the right-hand term. For HCO⁺ and HNC, the dips of infrared absorption features,

f_{IR} , are at most <0.01 [Jy] and <0.1 [Jy], respectively (Fig. 10). The peak fluxes of the HCO^+ $v_2=1f$ J=3–2 and HNC $v_2=1f$ J=3–2 emission lines in the millimeter wavelength are <1.0 [mJy] and ~ 0.8 [mJy], respectively (Fig. 4). The upper limit and value in the left-hand term of Equation (22) is about three orders of magnitude larger than the right-hand term also for HCO^+ and HNC, respectively. Although the energy absorbed by the infrared photons is used for other J-transition lines at $v_2=1f$ for HCN/ HCO^+ /HNC, there is a large enough margin for infrared radiative pumping as the source of vibrational excitation of HCN/ HCO^+ /HNC, unless the actual strengths of the infrared $v_2=1$ absorption features of HCN/ HCO^+ /HNC are more than three orders of magnitude smaller than the current upper limits. The observed velocity widths of HCN and HNC $v_2=1f$ J=3–2 emission lines are ~ 200 km s $^{-1}$ in FWHM (Table 3). To detect absorption features with this level of velocity width, a spectral resolution with $R > 1500$ is necessary. The minimum required infrared absorption features of HCN/ HCO^+ /HNC are too weak to be detected with the current quality Spitzer IRS R ~ 600 spectrum. A higher S/N and spectral resolution spectrum is therefore required to unambiguously detect the infrared $v_2=1$ absorption features of HCN/ HCO^+ /HNC, and to better constrain the energetics between absorbed infrared photons and $v_2=1f$ J-transition emission lines more quantitatively.

In summary, it is very likely that infrared radiative pumping is at work in IRAS 20551–4250, and therefore the infrared radiative pumping effect must be properly taken into account for HCN and HNC, and possibly for HCO^+ too, if we are to understand rotational excitation at $v=0$ and J-transition flux ratio at $v=0$ in IRAS 20551–4250. However, based on the currently available data, it is not yet quantitatively clear what percentages of the observed molecular line fluxes at $v=0$ are altered by the infrared radiative pumping, compared to collisional excitation. Molecular gas rotational J-level populations and fluxes of rotational J-transitions at $v=0$ in IRAS 20551–4250 are determined by (a) collisional excitation, which is dependent on molecular gas physical parameters (density, kinetic temperature etc), and (b) contribution from infrared radiative pumping. Obtaining further molecular line data at other J-transition lines at both $v=0$ and $v_2=1$ will help to better disentangle these two factors and to better understand the physical origin of the observed HCN/ HCO^+ /HNC molecular line flux ratios in IRAS 20551–4250.

5. SUMMARY

We conducted ALMA Cycle 2 observations of the AGN-hosting ULIRG, IRAS 20551–4250, at HCN/ HCO^+ /HNC J=3–2 (rotational transition) at both vibrational-ground ($v=0$) and vibrationally excited ($v_2=1$) levels. Since our ALMA Cycle 0 observations showed a tentatively detectable ($\sim 5\sigma$) vibrationally excited HCN $v_2=1f$ J=4–3 emission line from this source, our new data are useful for investigating (a) whether the vibrationally excited ($v_2=1f$) HCN emission line is visible at J=3–2 as well, and (b) the strength of the vibrationally excited ($v_2=1f$) J=3–2 emission lines for HCO^+ and HNC. The main results of these observations are as follows:

1. HCN, HCO^+ , and HNC J=3–2 emission lines at vibrational-ground level were clearly detected at the continuum peak position.
2. We detected HCN $v_2=1f$ J=3–2 and HNC $v_2=1f$ J=3–2 emission lines, based on Gaussian fits of the spectra and integrated intensity (moment 0) maps, supporting the scenario that IRAS 20551–4250 shows detectable vibrationally excited $v_2=1f$ J-transition emission lines for both HCN and HNC.
3. The vibrationally excited HCO^+ $v_2=1f$ J=3–2 emission line was not clearly detected, but a stringent upper limit was in place. The observed $v_2=1f$ J=3–2 to $v=0$ J=3–2 flux ratio for HCO^+ is more than a factor of four smaller than those for HCN and HNC.
4. Since collisional excitation is very difficult to significantly populate the $v_2=1$ level, due to its high energy level (>600 K), we calculated how infrared radiative pumping can achieve the vibrational excitation, using the available infrared 5–35 μm spectrum. It was estimated that the infrared radiative pumping rate to $v_2=1$ of HCN is comparable to HCO^+ , but is smaller than HNC by more than an order of magnitude. Our observational results about the $v_2=1f$ J=3–2 emission line fluxes of HCN, HCO^+ , and HNC can naturally be explained, if the HCN abundance is greater than a factor of few higher than HCO^+ , and an order of magnitude higher than HNC. Because of the low observed equivalent widths of the PAH emission features at 5–25 μm , it was interpreted that infrared photons used for the vibrational excitation of HCN/ HCO^+ /HNC mostly come from AGN-heated hot dust emission near an AGN. Thus, the properties of molecular gas derived from the $v_2=1f$ emission largely reflect those of AGN-affected molecular gas in the close vicinity of an AGN. In fact, HCN abundance enhancement in the close vicinity of AGNs was argued in several previous works.
5. The observed $v_2=1f$ J=3–2 to $v=0$ J=3–2 flux ratios for HCN/ HCO^+ /HNC and the observed HCN $v=0$ J=3–2 to H^{13}CN $v=0$ J=3–2 flux ratio suggest that HCN $v=0$ J=3–2 emission has a significant line opacity and is flux-attenuated by a factor of 6, whereas the flux attenuation of HCO^+ $v=0$ J=3–2 and HNC $v=0$ J=3–2 emission lines was estimated to be <3 and ~ 1 , respectively. The higher flux attenuation by line opacity for HCN than HCO^+ and HNC is as expected from the estimated higher HCN abundance than HCO^+ and HNC.
6. The observed flux ratio and excitation temperature between $v_2=1f$ and $v=0$ suggest that infrared radiative pumping has an effect to rotational excitation at $v=0$ for HCN and HNC.
7. The HCN-to- HCO^+ J=3–2 flux ratio at $v=0$ is similar to the previously obtained HCN-to- HCO^+ J=4–3 flux ratio at $v=0$ in IRAS 20551–4250, and both are higher than starburst-dominated regions. The enhanced HCN-to- HCO^+ flux ratio

in this AGN-hosting ULIRG was interpreted to be originated mainly in the enhanced HCN-to-HCO⁺ abundance ratio and sufficient HCN excitation, rather than the substantially higher infrared radiative pumping efficiency of HCN than that of HCO⁺. When the estimated line opacity for HCN/HCO⁺/HNC $v=0$ emission is corrected, the HCN-to-HCO⁺ J=3–2 and HCN-to-HNC J=3–2 flux ratio at $v=0$ for IRAS 20551–4250 will increase, even deviating from the ratios found in starburst-dominated regions. If larger HCN line opacity due to enhanced HCN abundance is common in AGNs, AGNs and starburst galaxies will be separated even more in the plot of line-opacity-corrected, intrinsic HCN-to-HCO⁺ and HCN-to-HNC flux ratios, than in the plot of observed flux ratios. Line opacity correction of other sources is also necessary to refine these molecular line flux ratios for use as an even more solid energy diagnostic method of dust/gas-rich ULIRGs.

8. Various emission lines, other than the targeted HCN/HCO⁺/HNC, were also detected, including HOC⁺, SO₂, SO, H¹³CN, HC₃N, and CH₃CCH, demonstrating the high sensitivity of ALMA and the abundant presence of excited molecular gas by

the nuclear energy source in IRAS 20551–4250.

We are grateful to the anonymous referee for his/her useful comments. We thank Dr. H. Nagai for his kind advice regarding ALMA data analysis, and Dr. K. Sakamoto for useful discussions. M.I. was supported by JSPS KAKENHI Grant Number 23540273 and 15K05030, and the ALMA Japan Research Grant of the NAOJ Chile Observatory, NAOJ-ALMA-0001 and -0023. T. I. is thankful for the fellowship received from the Japan Society for the Promotion of Science (JSPS). This paper makes use of the following ALMA data: ADS/JAO.ALMA#2013.1.00033.S. ALMA is a partnership of ESO (representing its member states), NSF (USA) and NINS (Japan), together with NRC (Canada), NSC and ASIAA (Taiwan), and KASI (Republic of Korea), in cooperation with the Republic of Chile. The Joint ALMA Observatory is operated by ESO, AUI/NRAO and NAOJ. This research has made use of NASA's Astrophysics Data System and the NASA/IPAC Extragalactic Database (NED) which is operated by the Jet Propulsion Laboratory, California Institute of Technology, under contract with the National Aeronautics and Space Administration.

REFERENCES

- Aalto, S., Booth, R. S., Black, J. H., & Johansson, L. E. B. 1995, *A&A*, 300, 369
- Aalto, S., Costagliola, S., Martin F., et al. 2015b, *A&A*, 584, 42
- Aalto, S., Garcia-Burillo, S., Muller, S., et al. 2015a, *A&A*, 574, A85
- Aalto, S., Spaans, M., Wiedner, M. C., & Huttemeister, S. 2007, *A&A*, 464, 193
- Amano, T., 1983, *J. Chem. Phys.*, 79, 7
- Antonucci, R. R. J. & Millar, J. S. 1985, *ApJ*, 297, 621
- Apponi, A. J., Pesch, T. C., & Ziurys, L. M. 1999, *ApJ*, 519, L89
- Apponi, A. J., & Ziurys, L. M. 1997, *ApJ*, 481, 800
- Baan, W. A., Henkel, C., Loenen, A. F., Baudry, A., & Wiklind, T. 2008, *A&A*, 477, 747
- Bardeen, J. M. 1970, *Nature*, 226, 64
- Bigiel, F., & Blitz, L. 2012, *ApJ*, 756, 183
- Blake, G. A., Sutton, E. C., Masson, C. R., & Phillips, T. G. 1986, *ApJS*, 60, 357
- Burkholder, J. B., Sinha, A., Hammer, P. D., & Howard, C. J. 1987, *Journal of Molecular Spectroscopy*, 126, 72
- Carroll, T. J., & Goldsmith, P. F., 1981, *ApJ*, 245, 891
- Costagliola, F., & Aalto, S. 2010, *A&A*, 515, A71
- Costagliola, F., Aalto, S., Rodriguez, M. I., et al., 2011, *A&A*, 528, A30
- Costagliola, F., Aalto, S., Sakamoto, K., et al. 2013, *A&A*, 556, 66
- Costagliola, F., Sakamoto, K., Muller, S., et al. 2015, *A&A*, 582, A91
- Davies, P. B., Hamilton, P. A., & Rothwell, W. J. 1984, *J. Chem. Phys.*, 81, 1598
- Debuhr, J., Quataert, E., & Ma, C-P. 2011, *MNRAS*, 412, 1341
- Deguchi, S., Claussen, M. J., & Goldsmith, P. F. 1986, *ApJ*, 303, 810
- Duc, P. -A., Mirabel, I. F., & Maza, J. 1997, *A&AS*, 124, 533
- Evans, A. S., Becklin, E. E., Scoville, N. Z., et al. 2003, *AJ*, 125, 2341
- Farrah, D., Serjeant, S., Efstathiou, A., Rowan-Robinson, M., & Verma, A. 2002, *MNRAS*, 336, 1163
- Farrah, D., Afonso, J., Efstathiou, A., et al. 2003 *MNRAS* 343 585
- Ferrarese, L., & Merritt, D. 2000, *ApJ*, 539, L9
- Foster, S. C., & McKellar, A. R. W., 1984, *J. Chem. Phys.*, 81, 3424
- Foster, S. C., McKellar, A. R. W., & Sears, T. J., 1984, *J. Chem. Phys.*, 81, 1
- Franceschini, A., Baito, V., Persic, M., et al. 2003, *MNRAS*, 343, 1181
- Fritz, T. K., Gillessen, S., Dodds-Eden, K., et al. 2011, *ApJ*, 737, 73
- Garcia-Burillo, S., Gracia-Carpio, J., Guelin, M., et al. 2006, *ApJ*, 645, L17
- Garcia-Burillo, S., Combes, F., Usero, A., et al. 2014, *A&A*, 567, 125
- Genzel, R. et al. 1998, *ApJ*, 498, 579
- Gierens, K. M., Stutzki, J., & Winnewisser, G. 1992, *A&A*, 259, 271
- Godard, B., Falgarone, E., Gerin, M., Hily-Blant, P., & De Luca, M., 2010, *A&A*, 520, A20
- Goldsmith, P. F., & Langer, W. D. 1999, *ApJ*, 517, 209
- Gracia-Carpio, J., Garcia-Burillo, S., Planesas, P., & Colina, L., 2006, *ApJ*, 640, L135
- Graninger, D. M., Herbst, E., Öberg, K. I., & Vasyunin, A. I., 2014, *ApJ*, 787, 74
- Greaves, J. S., & White, G. J. 1991, *A&AS*, 91, 237
- Greve, T. R., Papadopoulos, P. P., Gao, Y., & Radford, S. J. E., 2009, *ApJ*, 692, 1432
- Gultekin, K., Richstone, D. O., Gebhardt, K., et al. 2009, *ApJ*, 698, 198
- Harada, N., Herbst, E., & Wakelam, V. 2010, *ApJ*, 721, 1570
- Harada, N., Thompson, T. A., & Herbst, E. 2013, *ApJ*, 765, 108
- Henkel, C., Asiri, H., Ao, Y., et al. 2014, *A&A*, 565, A3
- Henkel, C., & Mauersberger, R. 1993, *A&A*, 274, 730
- Henkel, C., Mauersberger, R., Wiklind, T., et al. 1993, *A&A*, 268, L17
- Hirota, T., Yamamoto, S., Mikami, H., & Ohishi, M., 1998, *ApJ*, 503, 717
- Hopkins, P. F., Hernquist, L., Cox, T. J., et al. 2005, *ApJ*, 630, 705
- Hopkins, P. F., Hernquist, L., Cox, T. J., et al. 2006, *ApJS*, 163, 1
- Hopkins, P. F., Hernquist, L., Cox, T. J., & Keres, D. 2008, *ApJS*, 175, 356
- Imanishi, M. 2009, *ApJ*, 694, 751
- Imanishi, M., & Dudley, C. C. 2000, *ApJ*, 545, 701
- Imanishi, M., Dudley, C. C., Maiolino, R., Maloney, P. R., Nakagawa, T., & Risaliti, G. 2007b, *ApJS*, 171, 72
- Imanishi, M., Imase, K., Oi, N., & Ichikawa, K. 2011, *AJ*, 141, 156
- Imanishi, M., Maiolino, R., & Nakagawa, T. 2010b, *ApJ*, 709, 801
- Imanishi, M., Nakagawa, T., Shirahata, M., Ohshima, Y., & Onaka, T. 2010a, *ApJ*, 721, 1233
- Imanishi, M., & Nakanishi, K. 2006, *PASJ*, 58, 813
- Imanishi, M., & Nakanishi, K. 2013a, *AJ*, 146, 47
- Imanishi, M., & Nakanishi, K. 2013b, *AJ*, 146, 91

- Imanishi, M., & Nakanishi, K. 2014, *AJ*, 148, 9
- Imanishi, M., Nakanishi, K., et al. 2016, in preparation
- Imanishi, M., Nakanishi, K., Kuno, N., & Kohno, K. 2004, *AJ*, 128, 2037
- Imanishi, M., Nakanishi, K., & Kohno, K. 2006, *AJ*, 131, 2888
- Imanishi, M., Nakanishi, K., Tamura, Y., Oi, N., & Kohno, K. 2007a, *AJ*, 134, 2366
- Imanishi, M., Nakanishi, K., Tamura, Y., & Peng, C. -H. 2009a, *AJ*, 137, 3581
- Iono, D., Saito, T., Yun, M. S., et al. 2013, *PASJ*, 65, L7
- Izumi, T., Kohno, K., Martin, S., Espada, D., Harada, N., et al. 2013, *PASJ*, 65, 100
- Izumi, T., Kohno, K., Aalto, S., et al. 2015, *ApJ*, 811, 39
- Izumi, T., Kohno, K., Aalto, S., et al. 2016, *ApJ*, 818, 42
- Kauffmann, G., Heckman, T. M., Tremonti, C., et al. 2003, *MNRAS*, 346, 1055
- Kawaguchi, K., Yamada, C., Saito, S., & Hirota, E., 1985, *J. Chem. Phys.*, 82, 1750
- Kewley, L. J., Heisler, C. A., Dopita, M. A., & Lumsden, S. 2001, *ApJS*, 132, 37
- Kohno, K. 2005, in *AIP Conf. Ser.* 783, *The Evolution of Starbursts*, ed. S. Hüttemeister, E. Manthey, D. Bomans, & K. Weis (New York: AIP), 203 (astro-ph/0508420)
- Komatsu, E., Dunkley, J., Nolte, M. R., et al. 2009, *ApJS*, 180, 330
- Krips, M., Neri, R., Garcia-Burillo, S., Martin, S., Combes, F., Gracia-Carpio, J., & Eckart, A. 2008, *ApJ*, 677, 262
- Lahuis, F., Spoon, H. W. W., Tielens, A. G. G. M., et al. 2007, *ApJ*, 659, 296
- Lebouteiller, V., Barry, D. J., Goes, C., et al. 2015, *ApJS*, 218, 21
- Lintott, C., & Viti, S. 2006, *ApJ*, 646, L37
- Liu, X-L., Wang, J-J., & Xu, J-L. 2013, *MNRAS*, 431, 27
- Magorrian, J., Tremaine, S., Richstone, D., et al. 1998, *ApJ*, 115, 2285
- Martin, S., Aalto, S., Sakamoto, K., et al. 2016, *A&A* in press (arXiv:1603.01291)
- Martin, S., Aladro, R., Martin-Pintado, J., & Mauersberger, R. 2010, *A&A*, 522, A62
- Mauclaire, G., Lemaire, J., Heninger, M., et al. 1995, *International Journal of Mass Spectrometry and Ion Processes*, 149, 487
- McConnell, N. J. & Ma, C-P. 2013, *ApJ*, 764, 184
- Meijerink, R., & Spaans, M. 2005, *A&A*, 436, 397
- Meijerink, R., Spaans, M., & Israel, F. P. 2007, *A&A*, 461, 793
- Mills, E. A. C., Güsten, R., Requena-Torres, M. A., & Morris, M. R., 2013, *ApJ*, 779, 47
- Moorwood, A. F. M. 1986, *A&A*, 166, 4
- Müller, H. S. P., Schlöder, F., Stutzki, J., Winnewisser, G. 2005, *J. Mol. Struct.*, 742, 215
- Nagy, Z., van der Tak, F. F. S., Fuller, G. A., & Plume, R. 2015, *A&A*, 577, A127
- Nakanishi, K., Okumura, S. K., Kohno, K., Kawabe, R., & Nakagawa, T. 2005, *PASJ*, 57, 575
- Nardini, E., Risaliti, G., Salvati, M., et al. 2008, *MNRAS*, 385, L130
- Nardini, E., Risaliti, G., Salvati, M., et al. 2009, *MNRAS*, 399, 1373
- Nardini, E., Risaliti, G., Watabe, Y., Salvati, M., & Sani, E. 2010, *MNRAS*, 405, 2505
- Nishiyama, S., Nagata, T., Tamura, M., et al. 2008, *ApJ*, 680, 1174
- Nishiyama, S., Tamura, M., Hatano, H., et al. 2009, *ApJ*, 696, 1407
- Petry, D., & CASA Development Team, 2012, in *ASP Conf. Ser.* 461, *Astronomical Data Analysis Software and Systems XXI*, ed. P. Ballester, D. Egret, & N. P. F. Lorente (San Francisco, CA: ASP), 849
- Privon, G. C., Herrero-Illana, R., Evans, A. S., et al. 2015, *ApJ*, 814, 39
- Prouton, O. R., Bressan, A., Clemens, M., et al. 2004, *A&A*, 421, 115
- Ranalli, P., Comastri, A., & Setti, G. 2003, *A&A*, 399, 39
- Rangwala, N., Maloney, P. R., Glenn, J., et al. 2011, *ApJ*, 743, 94
- Risaliti, G., Maiolino, R., Marconi, A., et al. 2006, *MNRAS*, 365, 303
- Roche P. F., & Aitken D. K. 1984, *MNRAS*, 208, 481
- Roche P. F., & Aitken D. K. 1985, *MNRAS*, 215, 425
- Rothberg, B., & Joseph, R. D. 2004, *AJ*, 128, 2098
- Ruiz, A., Miniutti, G., Panessa, F., & Carrera, F. J., 2010, *A&A*, 515, A99
- Rybicki, G. B., & Lightman, A. P. 1979, *Radiative Processes in Astrophysics* (New York: Wiley)
- Saito, T., Iono, D., Yun, M. S., et al. 2015, *ApJ*, 803, 60
- Sakamoto, K., Aalto, S., Costagliola, F., et al. 2013, *ApJ*, 764, 42
- Sakamoto, K., Aalto, S., Evans, A. S., Wiedner, M., & Wilner, D. 2010, *ApJ*, 725, L228
- Sanders, D. B., Mazzarella, J. M., Kim, D. -C., Surace, J. A., & Soifer, B. T. 2003, *AJ*, 126, 1607
- Sani, E., Risaliti, G., Salvati, M., et al. 2008, *ApJ*, 675, 96
- Sargsyan, L., Weedman, D., Lebouteiller, V., et al. 2011, *ApJ*, 730, 19
- Savage, C., & Ziurys, L. M., 2004, *ApJ*, 616, 966
- Schilke, P., Walmsley, C. M., Pineau des Forets, G., et al. 1992, *A&A*, 256, 595
- Shang, Z., Brotherton, M. S., Wills, B. J., et al. 2011, *ApJ*, 196, 2
- Snell, R. L., Narayanan, G., Yun, M. S., et al. 2011, *ApJ*, 141, 38
- Solomon, P. M., Scoville, N. Z., & Sanders, D. B. 1979, *ApJ*, 232, L89
- Solomon, P. M., Rivolo, A. R., Barrett, J., et al. 1987, *ApJ*, 319, 730
- Solomon, P. M., & Vanden Bout, P. A. 2005, *ARA&A*, 43, 677
- Spoon, H. W. W., Keane, J. V., Tielens, A. G. G. M., Lutz, D., & Moorwood, A. F. M. 2001, *A&A*, 365, L353
- Stock, D. J., Peeters, E., Choi, W. D. -Y., & Shannon, M. J. 2014, *ApJ*, 791, 99
- Thorne, K. S. 1974, *ApJ*, 191, 507
- Townes, C. H., & Schawlow, A. L., 1975, *Microwave Spectroscopy*
- Ueda, J., Iono, D., Yun, M. S., et al. 2014, *ApJS*, 214, 1
- Veatch, T. J., Groppi, C., & Hedded, A., 2013, *ApJ*, 765, L34
- Vega, O., Clemens, M. S., Bressan, A., et al. 2008, *A&A*, 484, 631
- Veilleux, S., & Osterbrock, D. E. 1987, *ApJS*, 63, 295
- Veilleux, S., Melendez, M., Sturm, E., et al. 2013, *ApJ*, 776, 27
- Voit, G. M. 1992, *MNRAS*, 258, 841
- Weiss, A., Downes, D., Neri, R., et al. 2007, *A&A*, 467, 955
- Yamada, M., Wada, K., & Tomisaka, K. 2007, *ApJ*, 671, 73
- Yuan, T. -T., Kewley, L. J., & Sanders, D. B. 2010, *ApJ*, 709, 884
- Ziurys, L. M., & Turner, B. E. 1986, *ApJ*, 300, L19

TABLE 1
LOG OF OUR ALMA CYCLE 2 OBSERVATIONS

Line (1)	Date (UT) (2)	Antenna Number (3)	Baseline (m) (4)	Integration time (min) (5)	Bandpass (6)	Calibrator Flux (7)	Phase (8)
HCN/HCO ⁺ J=3–2	2014 May 17	35	15–650	14	J2056–4714	J2056–4714	J2056–4714
HNC J=3–2	2014 May 17	35	15–650	36	J2056–4714	J2056–4714	J2056–4714

NOTE. — Col.(1): Observed line. Col.(2): Observation date (UT). Col.(3): Number of antennas used for observations. Col.(4): Baseline length in meter. Minimum and maximum baseline lengths are shown. Col.(5): Net on-source integration time in minutes. Cols.(6), (7), and (8): Bandpass, flux, and phase calibrator for the target source, respectively. The flux density of J2056–4714 is estimated from ALMA monitoring observations.

TABLE 2
CONTINUUM EMISSION

Frequency [GHz] (1)	Flux [mJy beam ^{−1}] (2)	Peak Coordinate (RA,DEC)J2000 (3)	rms [mJy beam ^{−1}] (4)	Synthesized beam [arcsec × arcsec] (°) (5)
a: 244.8–246.6, 247.1–249.0, 259.8–263.5	3.8 (59σ)	(20 58 26.80, −42 39 00.3)	0.065	0.50×0.46 (74°)
b: 254.0–258.5	3.6 (88σ)	(20 58 26.80, −42 39 00.3)	0.041	0.52×0.47 (66°)

NOTE. — Col.(1): Frequency range in [GHz] used for extraction of continuum-a (taken simultaneously with HCN and HCO⁺ J=3–2 observations), and -b (obtained at the same time as HNC J=3–2 observations). Frequencies at obvious emission line features are removed. Col.(2): Flux in [mJy beam^{−1}] at the emission peak. Value at the highest flux pixel (0''.1 pixel^{−1}) is extracted. The detection significance relative to the rms noise is shown in parentheses. Possible systematic uncertainty is not included. Col.(3): The coordinate of the continuum emission peak in J2000. Col.(4): The rms noise level (1σ) in [mJy beam^{−1}]. Col.(5): Synthesized beam in [arcsec × arcsec] and position angle in [degree]. The position angle is 0° along the north–south direction and increases in the counterclockwise direction.

TABLE 3
MOLECULAR LINE FLUX

Line (1)	ν_{rest} [GHz] (2)	Integrated intensity (moment 0) map				Velocity [km s ⁻¹] (7)	Gaussian line fit		Flux [Jy km s ⁻¹] (10)
		Peak [Jy beam ⁻¹ km s ⁻¹] (3)	rms (4)	Elements Summed (5)	Beam [" × " (°)] (6)		Peak [mJy] (8)	FWHM [km s ⁻¹] (9)	
HCN J=3-2	265.89	5.5 (85 σ)	0.064	16	0.49×0.46 (73°)	12894±1	31±1	187±2	5.9±0.1
HCO ⁺ J=3-2	267.56	8.0 (87 σ)	0.092	18	0.49×0.46 (75°)	12889±1	43±1	193±2	8.4±0.1
HCN J=3-2, $v_2=1f$	267.20	0.22 (7.6 σ)	0.029	9	0.49×0.46 (75°)	12883±12	1.5±0.2	165±34	0.25±0.07
HOC ⁺ J=3-2	268.45	0.18 (6.4 σ)	0.028	8	0.49×0.46 (74°)	12884±21	1.4±0.4	131±55	0.19±0.10
HCO ⁺ J=3-2, $v_2=1f$	268.69	<0.088 (<3 σ)	0.029	9	0.49×0.46 (74°)	—	—	—	—
HNC J=3-2	271.98	3.0 (86 σ)	0.035	14	0.50×0.47 (74°)	12895±2	19±1	164±3	3.2±0.1
HNC J=3-2, $v_2=1f$ ^a	273.87	0.17 (6.5 σ)	0.027	12	0.51×0.44 (66°)	12891±29	0.80±0.17	243±68	0.20±0.07
SO ₂ 5(3,3)-5(2,4)	256.25	0.48 (20 σ)	0.024	12	0.54×0.47 (65°)	12805±5	3.1±0.2	153±12	0.49±0.05
SO 6(6)-5(5)	258.26	0.48 (22 σ)	0.021	11	0.53×0.47 (63°)	12912±6	2.8±0.2	188±13	0.54±0.05
H ¹³ CN J=3-2	259.01	0.34 (12 σ)	0.028	15	0.53×0.47 (63°)	12884±9	1.7±0.2	205±22	0.37±0.05
HC ₃ N J=30-29	272.89	0.16 (9.2 σ)	0.017	8	0.50×0.47 (74°)	12900±13	1.1±0.2	166±32	0.19±0.05
CH ₃ CCH 16(2)-15(2)	273.40	0.59 (17 σ)	0.034	17	0.51×0.44 (66°)	12866±7	2.8±0.2	203±17	0.58±0.06

NOTE. — Col.(1): Observed molecular line. Molecular lines above the solid horizontal line were obtained simultaneously with continuum-a. Those below the line were taken at the same time as continuum-b. Col.(2): Rest-frame frequency of each molecular line in [GHz]. Col.(3): Integrated intensity in [Jy beam⁻¹ km s⁻¹] at the emission peak. Value at the highest flux pixel (0''.1 pixel⁻¹) is extracted. Detection significance relative to the rms noise (1 σ) in the moment 0 map is shown in parentheses. Possible systematic uncertainty is not included. Col.(4): rms noise (1 σ) level in the moment 0 map in [Jy beam⁻¹ km s⁻¹], derived from the standard deviation of sky signals in each moment 0 map. Col.(5): The number of spectral elements summed to create moment 0 maps. Each spectral element (~20 MHz width) consists of 40 correlator channels binning (see §2). Col.(6): Beam size in [arcsec × arcsec] and position angle in [degree]. Position angle is 0° along the north-south direction, and increases counterclockwise. Cols.(7)–(10): Gaussian fits of emission lines in the spectra at the continuum peak position, within the beam size. Col.(7): Optical LSR velocity (v_{opt}) of emission peak in [km s⁻¹]. Col.(8): Peak flux in [mJy]. Col.(9): Observed FWHM in [km s⁻¹] in Figure 4. Col.(10): Flux in [Jy km s⁻¹]. Possible systematic uncertainty is not included. The observed FWHM in [km s⁻¹] in column 9 is divided by (1 + z) to obtain the intrinsic FWHM in [km s⁻¹].

^a HNC $v_2=1f$ J=3-2 emission line could possibly be contaminated by HC₃N $v_7=1f$ J=30-29 line ($\nu_{\text{rest}}=273.94$ GHz) (Costagliola et al. 2013). Although the peak velocity of the HNC $v_2=1f$ J=3-2 emission line based on Gaussian fit is comparable to those of HCN, HCO⁺, and HNC $v=0$ J=3-2 emission lines, as well as the HCN $v_2=1f$ J=3-2 emission line, the line width is 25–50% larger, possibly indicating the contamination.

TABLE 4
MOLECULAR LINE LUMINOSITY FOR IRAS 20551–4250

Line (1)	[10 ⁴ L _⊙] (2)	[10 ⁷ K km s ⁻¹ pc ²] (3)
HCN J=3-2	5.5±0.1	9.2±0.2
HCO ⁺ J=3-2	7.9±0.1	12.9±0.2
HNC J=3-2	3.1±0.1	4.7±0.1
HCN J=3-2 $v_2=1f$	0.23±0.07	0.35±0.10
HCO ⁺ J=3-2 $v_2=1f$	<0.084	<0.13
HNC J=3-2 $v_2=1f$	0.19±0.07	0.27±0.09
HCN J=4-3	11.8±0.3	8.3±0.2
HCO ⁺ J=4-3	17.5±1.3	12.1±0.9
HNC J=4-3	7.4±0.3	4.8±0.2
HCN J=4-3 $v_2=1f$	0.49±0.09	0.34±0.06

NOTE. — Col.(1): Molecular line. Col.(2): Luminosity in units of [10⁴ L_⊙], calculated with equation (1) of Solomon & Vanden Bout (2005). Col.(3): Luminosity in units of [10⁷ K km s⁻¹ pc²], calculated with equation (3) of Solomon & Vanden Bout (2005). Luminosities at J=4-3 are also calculated from data by Imanishi & Nakanishi (2013b).

TABLE 5
PARAMETERS FOR MOLECULAR TRANSITION LINES

Line (1)	Frequency [GHz] (2)	E_u/k_B [K] (3)	A_{ul} [10^{-4} s^{-1}] (4)	Flux [Jy km s ⁻¹] (5)
HCN J=3–2	265.89	25.5	8.4	5.9±0.1
HCN J=3–2, $v_2=1f$	267.20	1050.0	7.3	0.25±0.07
HCO ⁺ J=3–2	267.56	25.7	14.5	8.4±0.1
HCO ⁺ J=3–2, $v_2=1f$	268.69	1217.4	13.1	<0.088
HNC J=3–2	271.98	26.1	9.3	3.2±0.1
HNC J=3–2, $v_2=1f$	273.87	692.0	8.5	0.20±0.07
HCN J=4–3	354.51	42.5	20.6	9.5±0.2
HCN J=4–3, $v_2=1f$	356.26	1067.1	19.0	0.39±0.07

NOTE. — Col.(1): Transition line. Col.(2): Rest-frame frequency in [GHz]. Col.(3): Upper energy level in [K]. Col.(4): Einstein A coefficient for spontaneous emission in [10^{-4} s^{-1}]. Values in Cols. (3) and (4) are from the Cologne Database of Molecular Spectroscopy (CDMS) (Müller et al. 2005) via Splatalogue (<http://www.splatalogue.net>). Col.(5): Flux in [Jy km s⁻¹] estimated based on Gaussian fits (Table 3, column 10). For the undetected HCO⁺ $v_2=1f$ J=3–2 emission line, an upper limit based on the integrated intensity (moment 0) map is adopted. HCN J=4–3 fluxes at $v_2=1f$ and $v=0$ are from Imanishi & Nakanishi (2013b).

TABLE 6
 $v_2=1f$ TO $v=0$ FLUX RATIO

Object (1)	Line (2)	Observed ratio (3)	Flux attenuation (4)	Intrinsic ratio (5)	Reference (6)
IRAS 20551–4250	HCN J=3–2	0.042	6	~0.01	This work
	HCO ⁺ J=3–2	<0.011	<3	<0.01	This work
	HNC J=3–2	0.063	~1	~0.06	This work
	HCN J=4–3	0.041	6	~0.01	Imanishi & Nakanishi (2013b)
NGC 4418	HCN J=4–3	0.23	~20	~0.01	Sakamoto et al. (2010)
	HCN J=3–2	0.17	~20	~0.01	Sakamoto et al. (2010)
Mrk 231	HCN J=3–2	0.042	~10	~0.005	Aalto et al. (2015a)

NOTE. — Col.(1): Object name. Only LIRGs with available quantitative information of flux attenuation for $v=0$ emission are shown. Col.(2): Molecular transition line. Col.(3): Ratio of the observed $v_2=1f$ to $v=0$ emission line flux in [Jy km s⁻¹]. Col.(4): Estimated flux attenuation for $v=0$ emission. The value of 6 means that flux is attenuated by line opacity with a factor of 6. Col.(5): Ratio of the intrinsic $v_2=1f$ to $v=0$ emission line flux in [Jy km s⁻¹], after line opacity correction of $v=0$ emission. Col.(6): Reference.

TABLE 7
SUMMARY OF THE RATIOS OF VARIOUS PARAMETERS FOR HCN, HCO⁺,
AND HNC

Parameters (1)	HCN : HCO ⁺ : HNC (2)
Column density at $v_2=1f$, J=3	1 : <0.20 : 0.69
Observed $v_2=1f$ to $v=0$ flux ratio at J=3–2	1 : <0.25 : 1.5
B coefficient from $v=0$ to $v_2=1$	1 : 1.1 : 11
Infrared flux used for vibrational excitation	1 : 0.8 : 2.5
Predicted infrared radiative pumping rate	1 : 0.9 : 27
Predicted $v_2=1$ to $v=0$ column density ratio	1 : 0.5 : 9
Derived abundance	1 : <0.4 : <0.08
Line opacity derived from isotopologue flux	1 : <0.5 : <0.2
Line opacity derived from abundance	1 : <0.7 : <0.1

NOTE. — Col.(1): Parameters used for our discussion in § 4.3. Col.(2): Ratio among HCN, HCO⁺, and HNC.

TABLE 8
EXCITATION TEMPERATURE FOR
IRAS 20551–4250

Molecule (1)	($v_2, J; v, J$) (2)	T_{ex} [K] (3)
HCN	(1f,3; 0,3)	340 (210)
	(1f,4; 0,4)	330 (210)
	(1f,3; 0,4)	430 (245)
	(1f,4; 0,3)	275 (185)
	(1f,4; 1f,3)	23
	(0,4; 0,3)	25
HNC	(1f,3; 0,3)	250
HCO ⁺	(1f,3; 0,3)	<270

NOTE. — Col.(1): Molecular line. Col.(2): Transition. Col.(3): Excitation temperature (T_{ex}) in [K]. For HCN $v=0$ $J=3-2$ and $J=4-3$ emission, flux attenuation with a factor of 6 is estimated (§4.3.2). In first four rows, T_{ex} values, after this correction by a factor of 6, are shown in the parentheses.

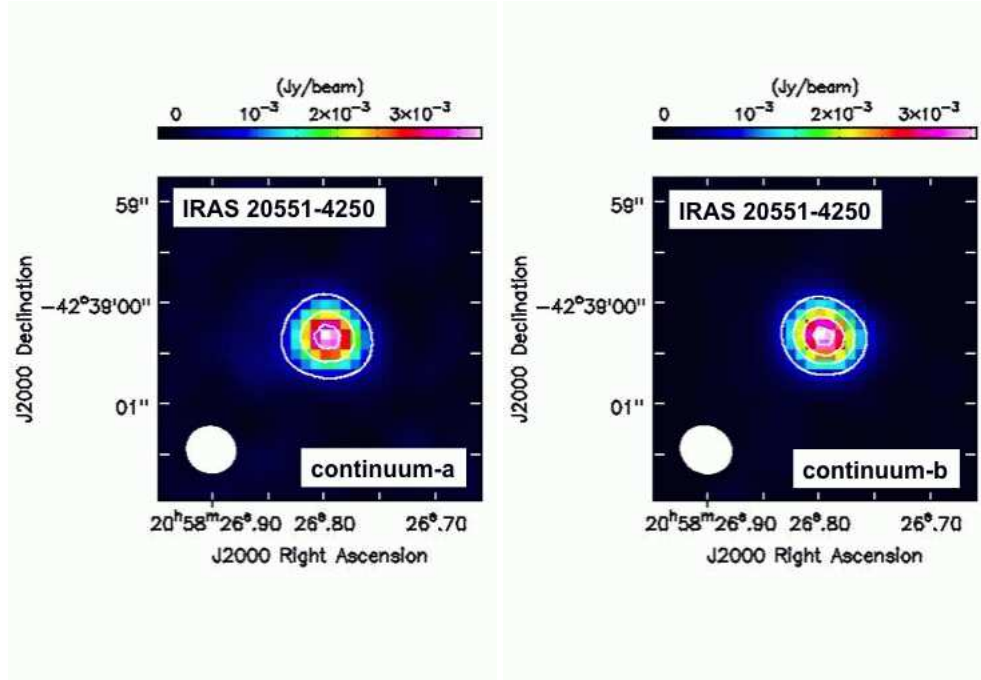


FIG. 1.— Continuum-a (central observed frequency $\nu_{\text{center}} \sim 256.3$ GHz) and -b ($\nu_{\text{center}} \sim 254.5$ GHz) data taken during the observations of HCN/HCO⁺ $J=3-2$ and HNC $J=3-2$, respectively. The contours represent the 10σ , 30σ , and 50σ levels for continuum-a and 20σ , 40σ , 60σ , and 80σ levels for continuum-b.

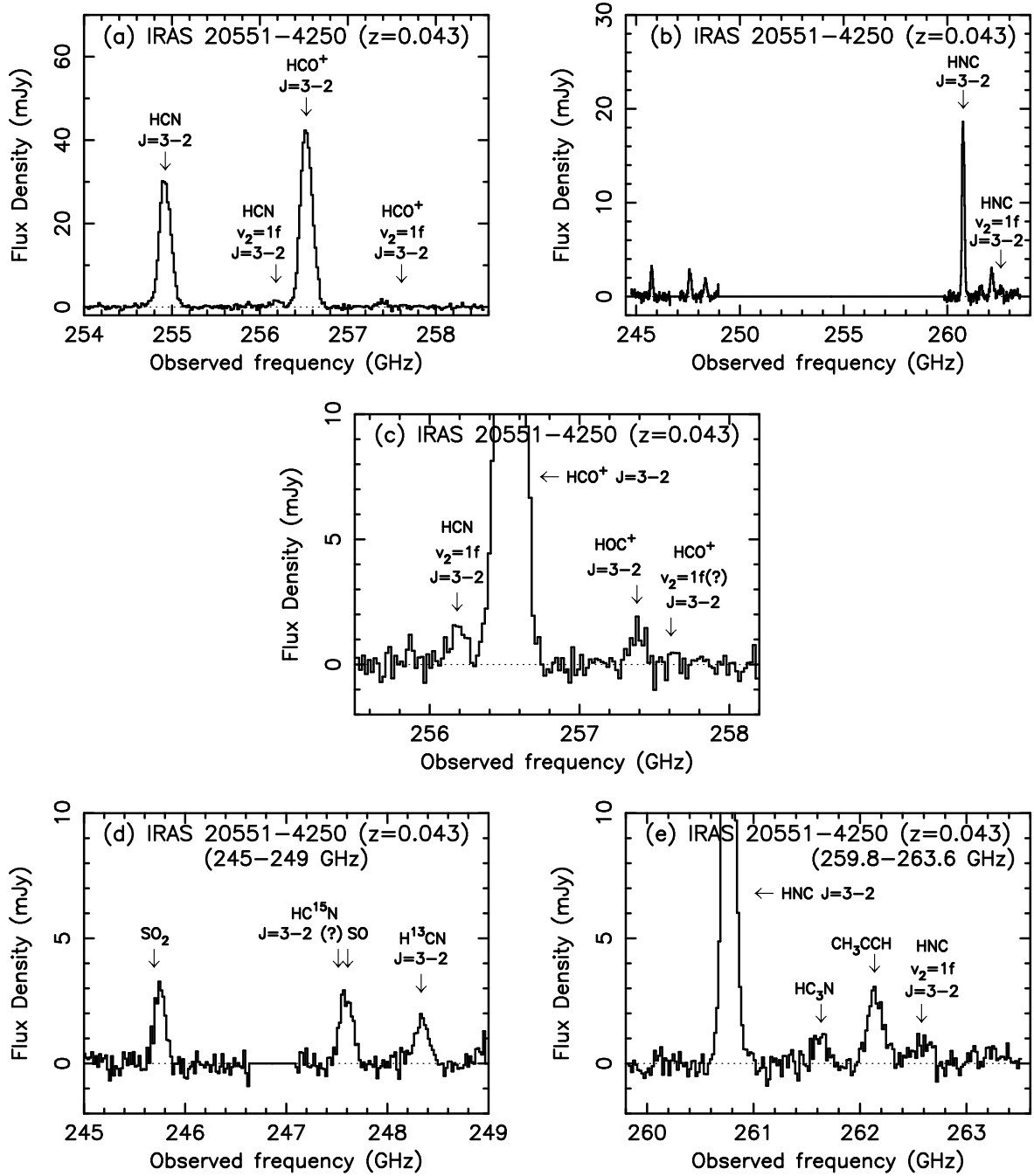
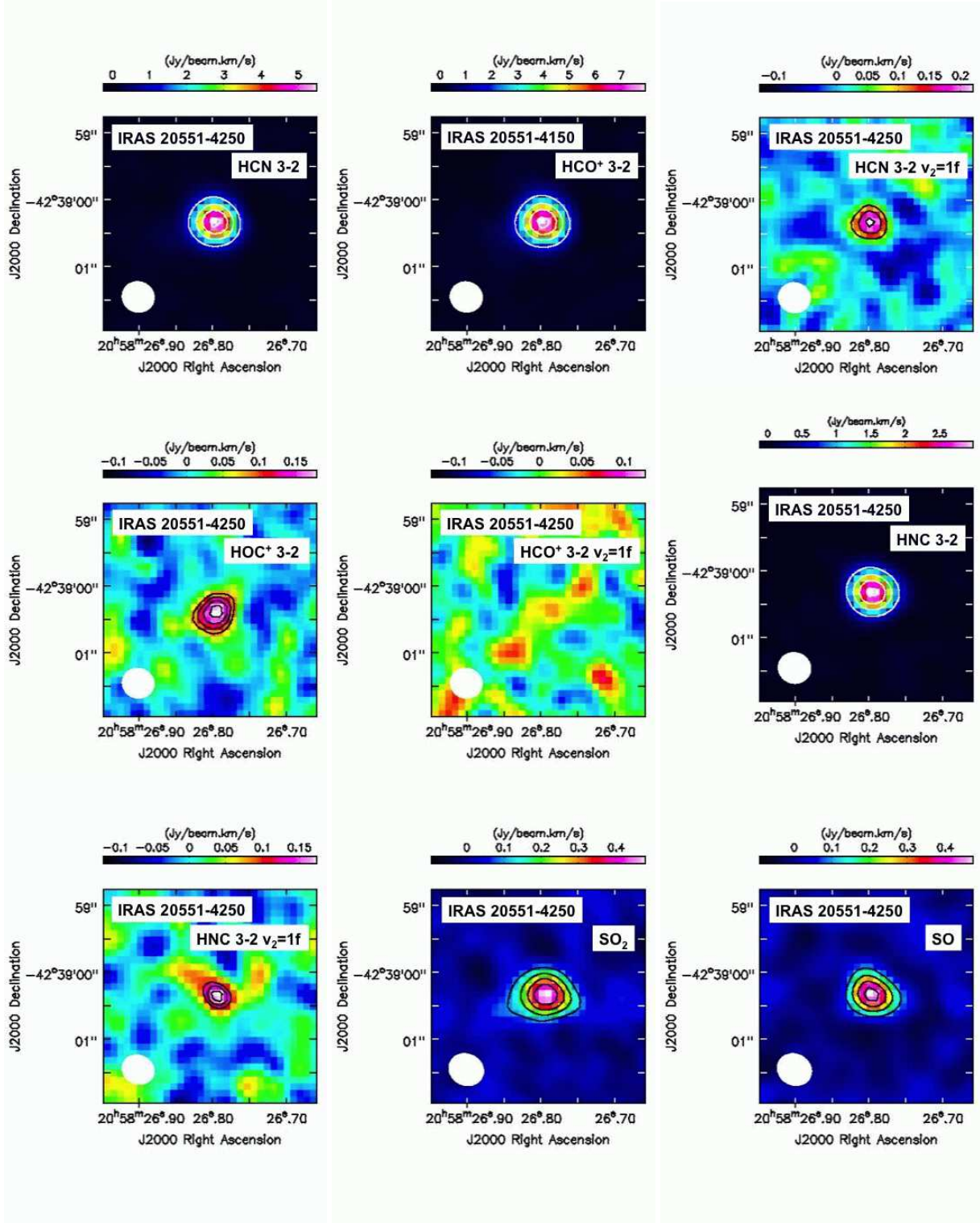


FIG. 2.— (a) : Full spectrum at the continuum peak position within the beam size for HCN/HCO⁺ J=3–2 observation. (b) : Full spectrum at the continuum peak position within the beam size for HNC J=3–2 observations. (c): Magnified spectrum around the HCO⁺ J=3–2 emission line, to display HCN $v_2=1f$ J=3–2 and HCO⁺ $v_2=1f$ J=3–2 lines. (d) : Magnified spectrum of lower frequency part for HNC J=3–2 observations, to show serendipitously detected emission lines in more detail. (e): Magnified spectrum of higher frequency part for HNC J=3–2 observations, to show serendipitously detected emission lines in more detail. The abscissa is the observed frequency in [GHz] and the ordinate is flux density in [mJy]. Down arrows are shown at the expected observed frequency for $z = 0.0430$, for individual molecular emission lines of our interest.



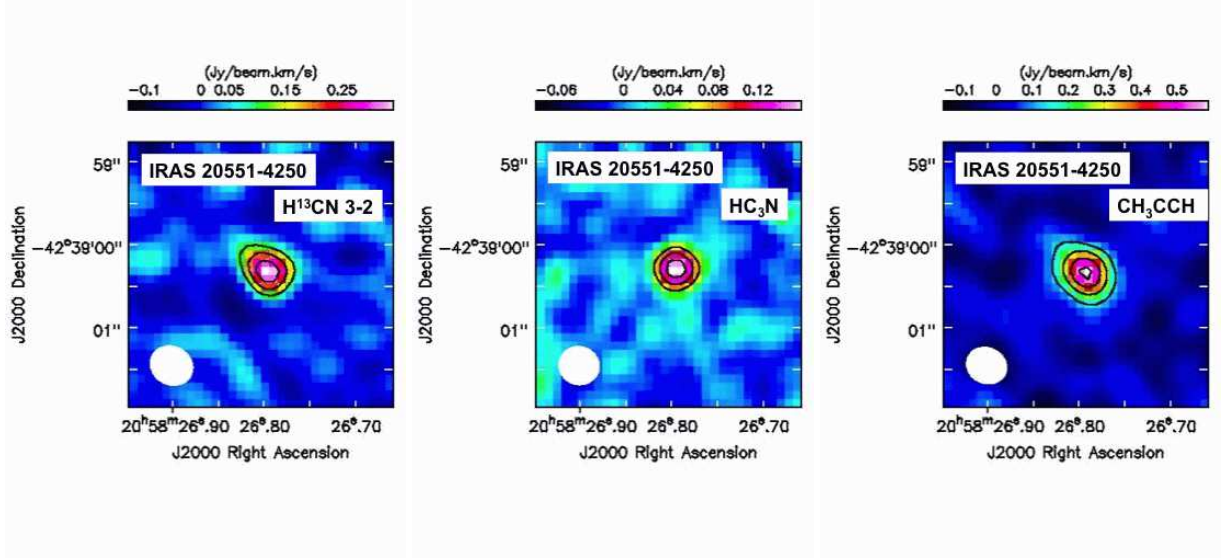


FIG. 3.— Integrated intensity (moment 0) maps of our interesting molecular lines in IRAS 20551–4250. The contours represent 20σ , 40σ , 60σ , 80σ for HCN J=3–2, 20σ , 40σ , 60σ , 80σ for HCO⁺ J=3–2, 3σ , 5σ , 7σ for HCN $v_2=1f$ J=3–2, 3σ , 4σ , 5σ , 6σ for HOC⁺ J=3–2, 20σ , 40σ , 60σ , 80σ for HNC J=3–2, 4σ , 5σ , 6σ for HNC $v_2=1f$ J=3–2, 4σ , 8σ , 12σ , 16σ for SO₂, 5σ , 10σ , 15σ , 20σ for SO, 4σ , 7σ , 10σ for H¹³CN J=3–2, 4σ , 6σ , 8σ for HC₃N, and 4σ , 8σ , 12σ , 16σ for CH₃CCH. For HCO⁺ $v_2=1f$ J=3–2, no emission with $\geq 3\sigma$ is found. The 1σ levels are different for different molecular lines. They are summarized in Table 3.

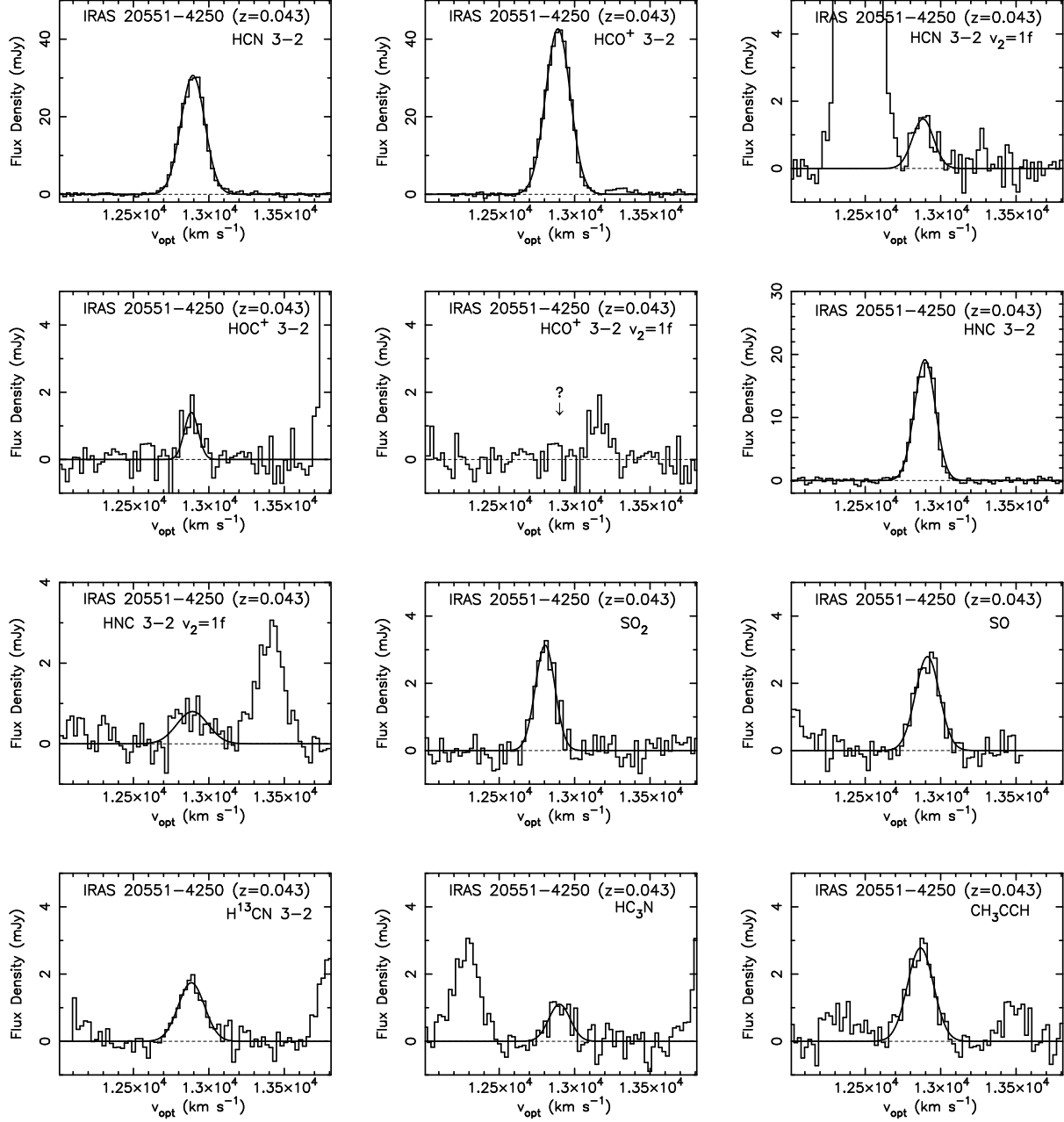


FIG. 4.— Spectra at the continuum peak position, within the beam size, of our interesting molecular lines in IRAS 20551-4250. All spectra are extracted at the continuum peak position at (20 58 26.80, -42 39 00.3)J2000. The abscissa is optical LSR velocity ($v_{\text{opt}} \equiv c(\lambda - \lambda_0)/\lambda_0$), and the ordinate is flux density in [mJy]. The best Gaussian fits (Table 3) are overplotted as solid curved lines.

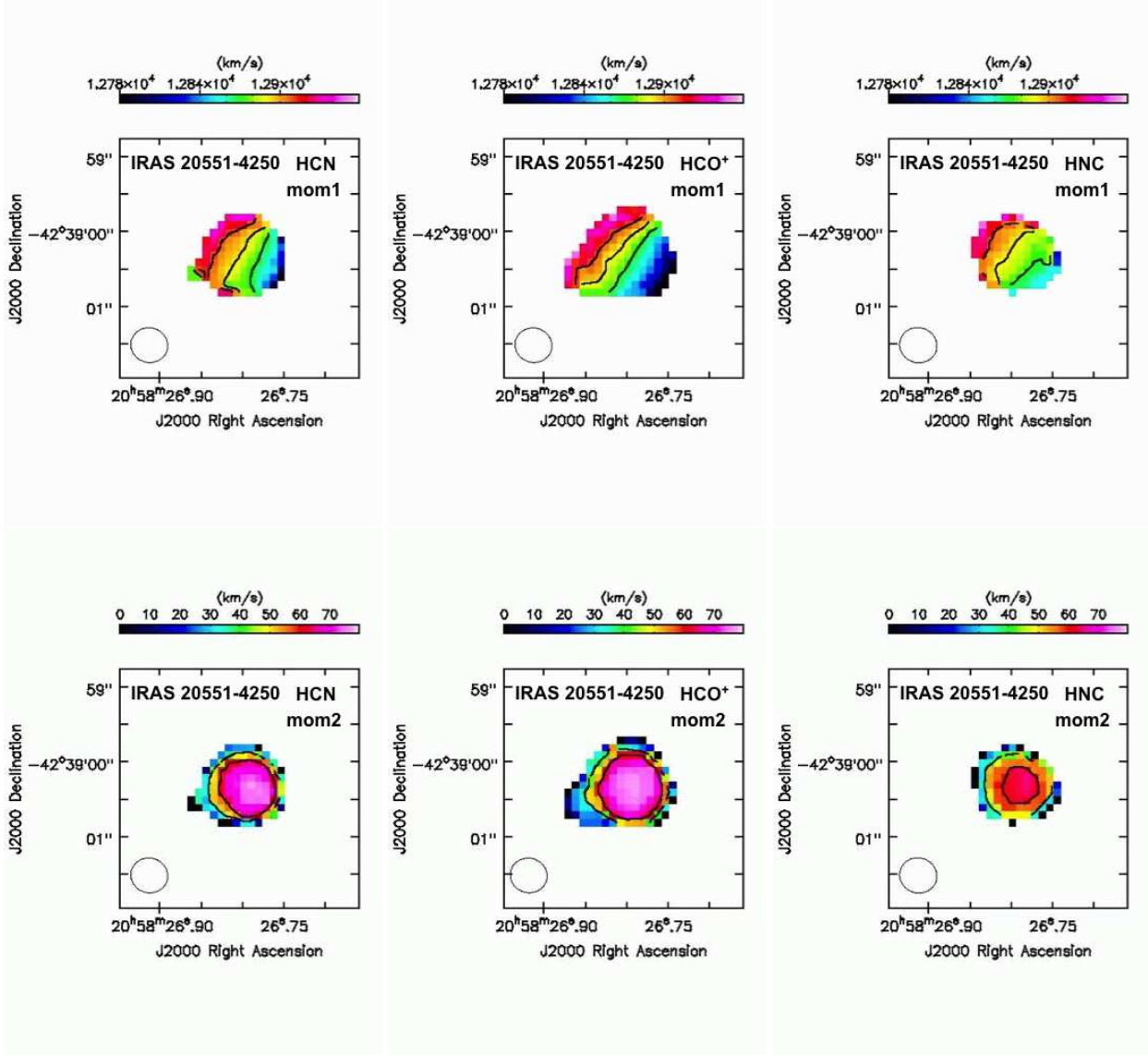


FIG. 5.— Intensity-weighted mean velocity (moment 1) and intensity-weighted velocity dispersion (moment 2) maps of HCN/HCO⁺/HNC J=3–2 ($v=0$) emission lines for IRAS 20551–4250. For moment 1 maps (top panels), the velocity is in optical LSR velocity ($v_{\text{opt}} \equiv c(\lambda - \lambda_0)/\lambda_0$). The contours in moment 1 maps are 12870, 12890, and 12910 km s^{−1} for HCN/HCO⁺/HNC J=3–2. The contours in moment 2 maps (bottom panels) are 40 and 60 km s^{−1} for HCN/HCO⁺/HNC J=3–2.

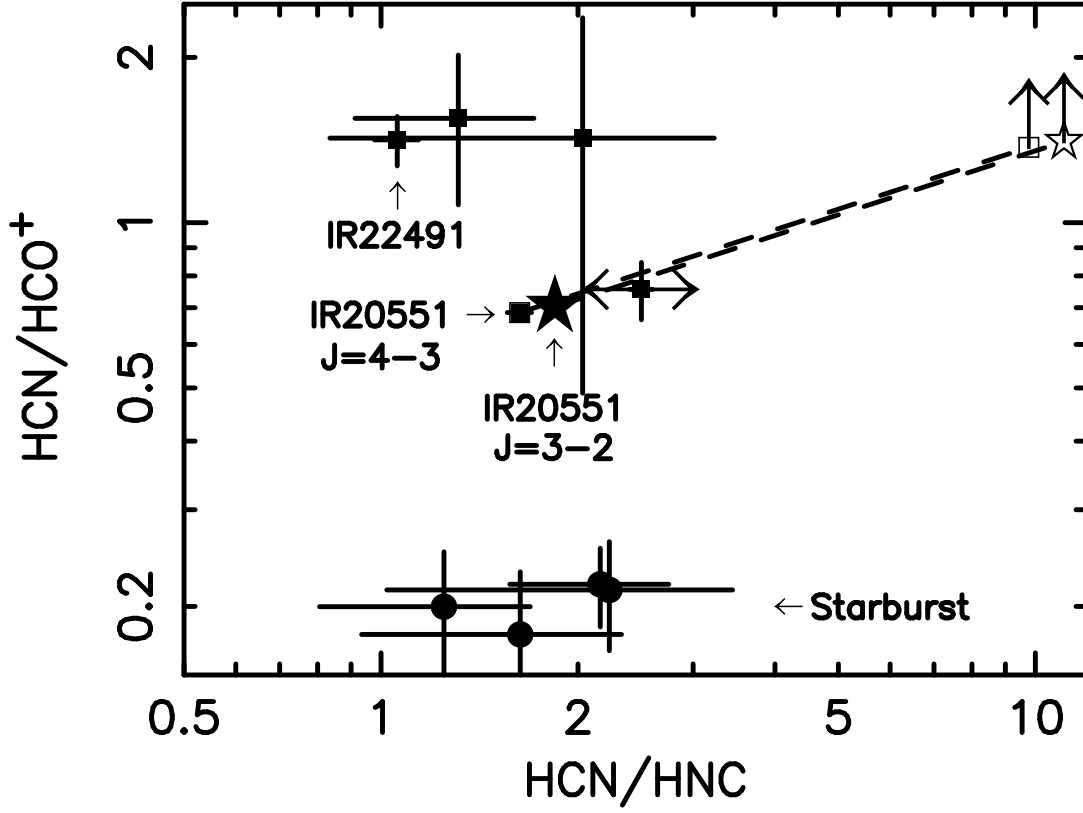


FIG. 6.— Observed HCN-to-HNC (abscissa) and HCN-to-HCO⁺ (ordinate) flux ratios, based on ALMA observations. The filled circles are J=4–3 data at multiple positions of the starburst-dominated LIRG, NGC 1614, taken by ALMA Cycle 0 observations (Imanishi & Nakanishi 2013a). The filled squares are J=4–3 data of ULIRGs, taken by ALMA Cycle 0 observations (Imanishi & Nakanishi 2013b, 2014). Although the ratios are unchanged, uncertainties are recalculated. All ULIRGs but one (IRAS 22491–1808) show infrared-identified energetically important buried AGNs (Imanishi & Nakanishi 2014). For IRAS 22491–1808, the HCN $v_2=1f$ J=3–2 emission line has been detected in our ALMA Cycle 2 data (Imanishi et al. 2016), suggesting that this ULIRG may contain an extremely buried AGN which is infrared-elusive but (sub)millimeter-detectable. The filled star is our new ALMA Cycle 2 J=3–2 data of IRAS 20551–4250. For IRAS 20551–4250, ratios after the correction for the derived line opacities (§4.3.2) are shown as the open square (J=4–3) and open star (J=3–2), which are connected to the observed ratios with the dashed lines.

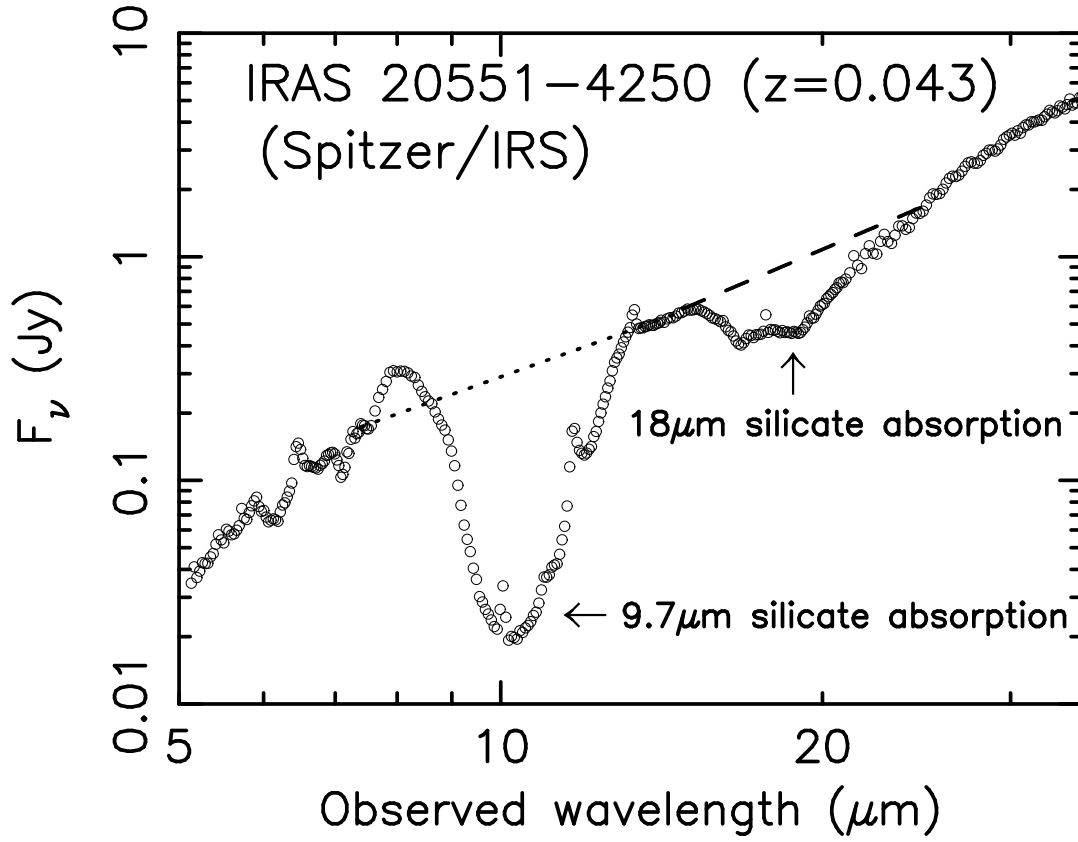


FIG. 7.— Spitzer IRS low-resolution ($R \sim 100$) infrared 5–35 μm spectrum of IRAS 20551–4250, originally shown by Imanishi et al. (2011), analyzed in the same manner as described in our previously published Spitzer IRS papers (Imanishi et al. 2007b; Imanishi 2009; Imanishi et al. 2010b). It is virtually identical to the spectrum shown by Sargsyan et al. (2011), except for small gaps among different spectral modules in the latter. Adopted power law continuum level for the 9.7 μm (18 μm) silicate dust absorption feature is determined, based on data points not strongly affected by these absorption features and polycyclic aromatic hydrocarbon (PAH) emission features (Imanishi et al. 2007b), and is overplotted as the dotted (dashed) line.

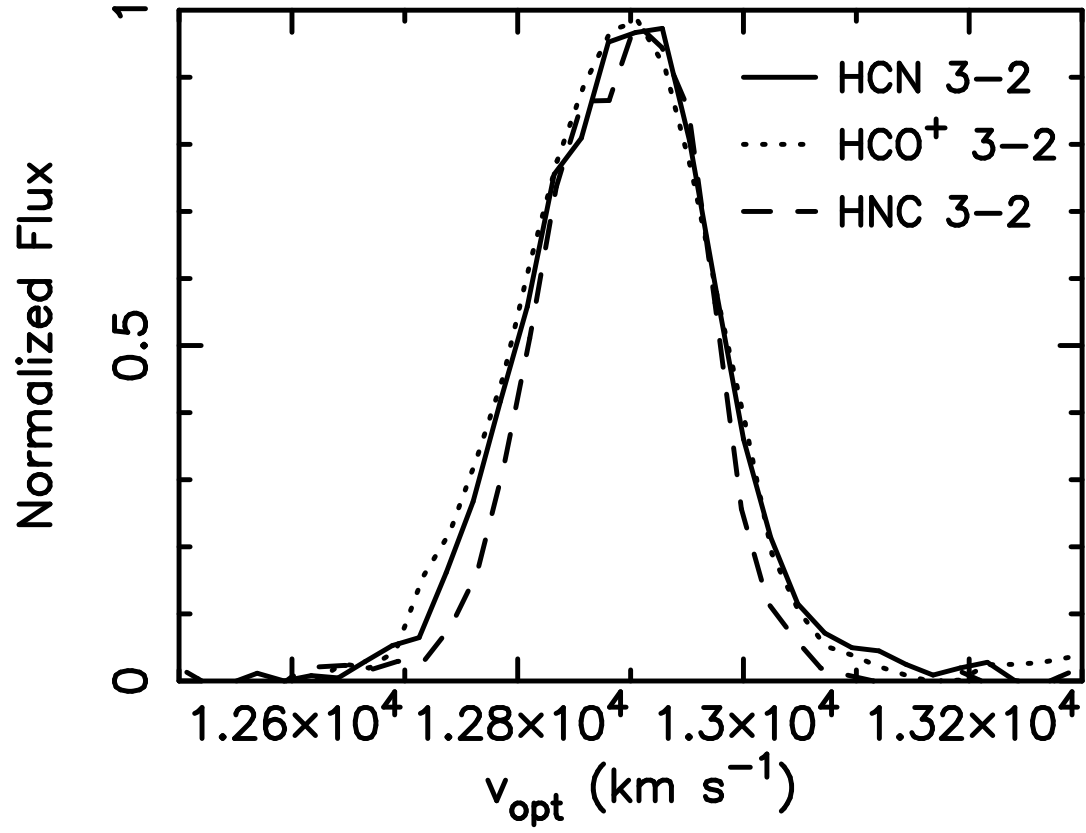


FIG. 8.— Comparison of the line profile of HCN J=3–2 (solid line), HCO $^+$ J=3–2 (dotted line), and HNC J=3–2 (dashed line) ($v=0$). The abscissa is optical LSR velocity ($v_{\text{opt}} \equiv c (\lambda - \lambda_0) / \lambda_0$), and the ordinate is flux normalized by the peak value of the Gaussian fits (Table 3, column 8).

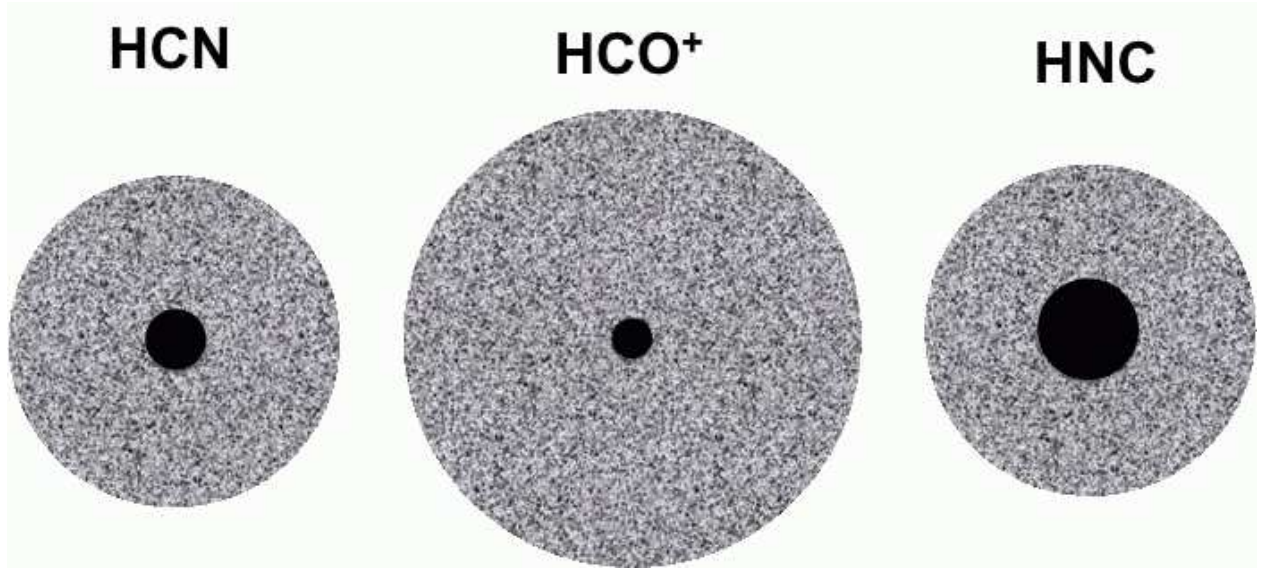


FIG. 9.— Schematic diagram of the spatial distribution of nuclear molecular gas and continuum emitting regions for infrared radiative pumping for HCN, HCO⁺, and HNC. The large gray circles are the expected sizes of HCN J=3–2, HCO⁺ J=3–2, and HNC J=3–2 ($v=0$) line emitting regions, assuming gradually decreasing radial density distribution of molecular gas from the very center to the outer region in a galaxy (Bigiel & Blitz 2012). The size is expected to be larger for HCO⁺ than HCN and HNC, due to a factor of ~ 5 lower critical density for HCO⁺ than HCN and HNC (see §4.4). It is likely that these regions consist of individual molecular gas clumps (see §4.3.2), and that HCO⁺ is less clumpy (occupies a larger volume fraction) than HCN and HNC, due to the lower HCO⁺ critical density (see §4.4). The central filled black circles represent infrared 14 μm (HCN), 12 μm (HCO⁺), 21.5 μm (HNC) continuum emitting regions. The size of the infrared continuum emitting region is expected to be the smallest for HCO⁺ and the largest for HNC. The bulk of the HCN/HCO⁺/HNC $v_2=1$ J=3–2 emission is likely to come from the inner region of the gray circle, where infrared radiation density from the central energy source is high (§4.4).

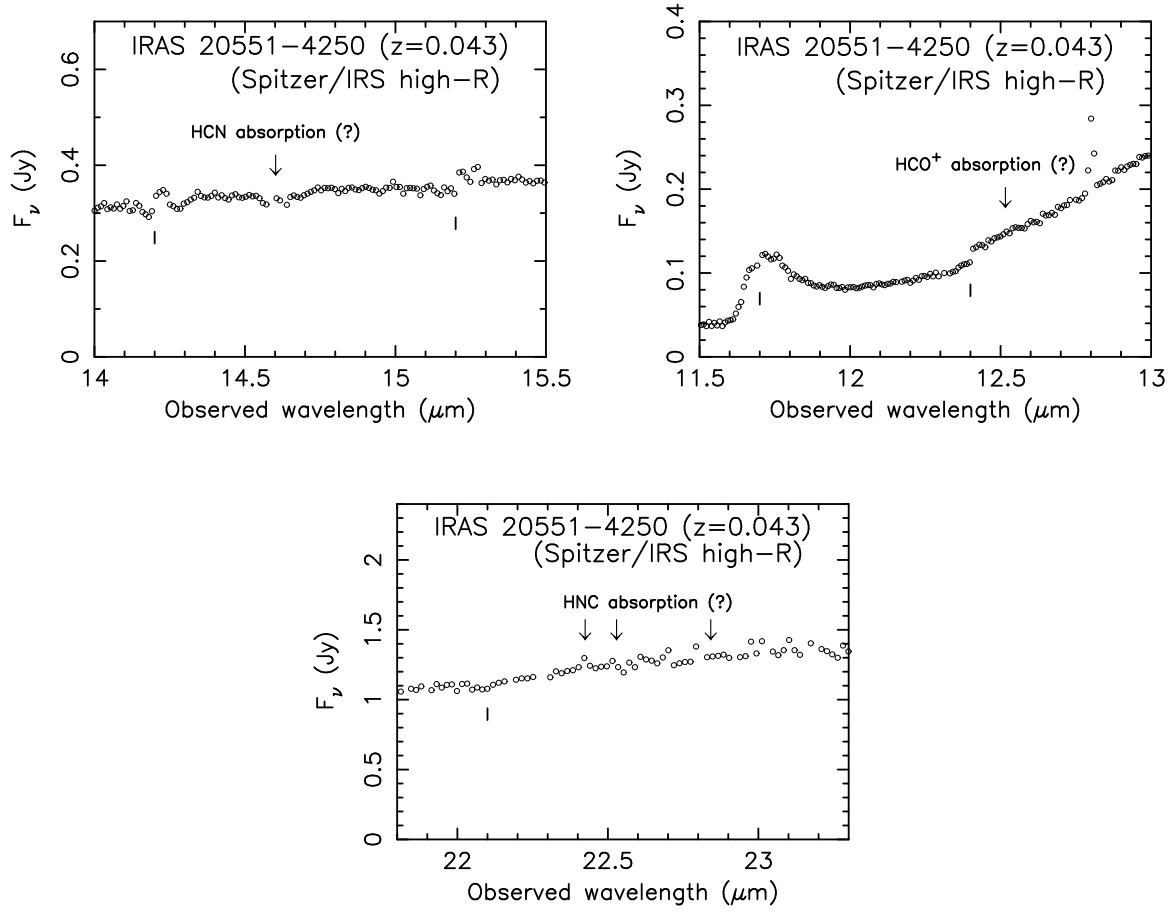


FIG. 10.— Spitzer IRS high-resolution ($R \sim 600$) infrared spectra of IRAS 20551–4250 taken from the Cornell Atlas of Spitzer/IRS Sources (CASSIS) (Lebouteiller et al. 2015). Zoom-in spectra around HCN, HCO^+ , and HNC absorption features at $\lambda_{\text{rest}} \sim 14 \mu\text{m}$, $12 \mu\text{m}$, and $21.5 \mu\text{m}$, respectively, are shown. For HCN and HCO^+ , down arrows are shown at $\lambda_{\text{rest}} = 14.0 \mu\text{m}$ and $12.0 \mu\text{m}$, respectively. For HNC, we plot down arrows at $\lambda_{\text{rest}} = 21.5 \mu\text{m}$, $21.6 \mu\text{m}$, and $21.9 \mu\text{m}$, which correspond to $v_2=1$ transition at low- J levels for R, Q, and P branches, respectively (Burkholder et al. 1987). Several small gaps seen in the spectra are due to observations with different spectral settings. These wavelengths at the edge of each spectral setting are indicated as the vertical solid straight lines.